

Use of Diffusion-Weighted MRI (DW-MRI) in the Management of Gynecological  
Cancer Patients Treated with EBRT and Brachytherapy

by

Julianna Schreiber Detrick  
Graduate Program in Medical Physics  
Duke University

Date: April 3, 2024

Approved:

Oana Craciunescu, Co-Advisor

Yongbok Kim, Co-Advisor

Chunhao Wang

Scott Robertson

Junzo Chino

Thesis submitted in partial fulfillment of  
the requirements for the degree of Master of Science in the Graduate Program in Medical  
Physics in the Graduate School of Duke University

2024

ABSTRACT

Use of Diffusion-Weighted MRI (DW-MRI) in Gross Tumor Volume (GTV) Delineation  
in Cervical Cancer Patients Undergoing Brachytherapy

by

Julianna Schreiber Detrick  
Graduate Program in Medical Physics  
Duke University

Date: April 3, 2024

Approved:

Oana Craciunescu, Co-Advisor

Yongbok Kim, Co-Advisor

Chunhao Wang

Scott Robertson

Junzo Chino

An abstract of a thesis submitted in partial fulfillment of  
the requirements for the degree of Master of Science in the Graduate Program in Medical  
Physics in the Graduate School of Duke University

2024

Copyright by  
Julianna Schreiber Detrick  
2024

## Abstract

**Purpose:** DW-MRI and its derived apparent diffusion coefficient (ADC) maps have shown promise in aiding the diagnosis and treatment of various cancer types. This study investigates the potential role of DW-MRI and ADC maps in GTV delineation for gynecological cancer patients undergoing external beam radiation therapy (EBRT) and brachytherapy. Additionally, longitudinal changes in DWI/ADC values were assessed throughout the course of brachytherapy.

**Methods:** Console-derived DW image sets and ADC maps were validated using an in-house MATLAB code. Optimization of the b-value, which defines the sensitivity of the imaging sequence to diffusion, was conducted quantitatively and qualitatively. After b-value optimization, GTV contouring was performed on three image sets; axial T2 MRI, axial T2 MRI fused with DWI at  $b=1300 \text{ s/mm}^2$ , and axial T2 MRI fused with ADC at  $b=0, 1000 \text{ s/mm}^2$ . Contour comparisons were made using the Hausdorff distance, Jaccard index, DICE coefficient, and mean pixel value. Finally, after applicator artifact quantification, a longitudinal analysis was performed examining the  $\text{CTV}_{\text{HRS}}$  throughout the course of brachytherapy on axial T2 MRI, DWI, and ADC maps.

**Results:** The optimal b-value was determined to be  $b=1300 \text{ s/mm}^2$ . Analysis of GTV delineation demonstrated that, for each patient, Dice coefficients and Jaccard indices from pre-EBRT scans were consistently greater than or equal to those from pre-BT scans. Also, only one out of the twelve cases resulted in ADC yielding the largest contoured volume. Also, in five out of six patients, the mean pixel value in the GTV contoured with

the help of DWI and with the help of ADC was greater and lower in pre-EBRT, respectively. The Jaccard indices, Hausdorff distances, and Dice coefficients of the contours done with the help of DWI and ADC were not significantly different ( $p=0.6384$ ,  $0.4354$ ,  $0.6550$ , respectively). The volumes of the  $GTV_{T2WS}$  were not significantly different than the GTVs done with the help of DWI and ADC, with  $p$ -values of  $0.4354$  and  $0.8729$ , respectively. The volumes contoured with the help of DWI were not significantly different to those contoured with the help of ADC ( $p=0.0989$ ).

No significant artifacts were observed outside of the tandem in the DW images and ADC maps. In the longitudinal analysis, a decreasing trend was observed across brachytherapy fractions in the DW images. Moreover, the average standard deviation of pixel values within each  $CTV_{HR}$ -tandem on the DW image set generally decreased throughout the course of brachytherapy. Regarding ADC maps, there was no apparent trend in the average of the mean pixel values. The average standard deviation generally increased across fractions, albeit to a small extent.

**Conclusion:** The results of this study indicate the potential of using ADC maps in tandem with axial T2 MRI to increase the accuracy of GTV delineation in GYN patients undergoing EBRT and brachytherapy. However, a larger sample size is needed to provide more insight into their use during the contouring workflow.

# Contents

Abstract.....	iv
List of Tables .....	viii
List of Figures.....	ix
Acknowledgements.....	xi
1. Introduction .....	1
1.1 Gynecological Cancer and the Role of Radiation Therapy .....	1
1.1.1 Role of EBRT.....	1
1.1.2 Role of Brachytherapy .....	2
1.1.2.1 High-Dose Rate (HDR) Brachytherapy .....	3
1.1.2.2 Low-Dose Rate (LDR) Brachytherapy .....	4
1.2 The Role of Imaging in Gynecological Malignancies .....	5
1.2.1 CT, PET, MRI.....	5
1.2.2 DWI/ADC Applications in Radiation Therapy.....	6
1.3 Artifacts in MRI Images Acquired for Brachytherapy .....	8
1.4 Clinical Radiation Therapy Treatment Workflow for GYN.....	9
1.5 Purpose.....	14
2. Materials and Methods.....	16
2.1 MRI Parameters, Patient Selection, and Patient Treatment .....	16
2.2 Diffusion-Weighted Magnetic Resonance Imaging (DW-MRI) .....	17
2.3 DW Image and ADC Map Validation .....	19
2.4 Optimization of b-Value .....	19
2.5 Gross Tumor Volume (GTV) Analysis.....	21

2.6 Applicator Artifact Quantification .....	24
2.7 Longitudinal Analysis of CTV <sub>HRS</sub> .....	25
3. Results .....	27
3.1 DW Image and ADC Map Validation .....	27
3.2 Optimization of b-Value .....	30
3.2.1 Quantitative Analysis .....	30
3.2.2 Qualitative Analysis .....	30
3.3 Gross Tumor Volume (GTV) Analysis .....	38
3.4 Applicator Artifact Quantification .....	44
3.5 Longitudinal Analysis of CTV <sub>HRS</sub> .....	46
4. Discussion .....	51
4.1 Optimization of b-Value .....	51
4.2 Gross Tumor Volume (GTV) Analysis .....	53
4.3 Applicator Artifact Quantification .....	55
4.4 Longitudinal Analysis of CTV <sub>HRS</sub> .....	55
4.4.1 Limitations .....	56
5. Conclusion .....	58
Appendix A .....	60
References .....	70

## List of Tables

Table 1: a) Tumor conspicuity rankings and their average values and b) total image quality rankings and their average values. ....	37
Table 2: Patient 1's individual data. Each statistic is written in the format of 'Pre-EBRT value, Pre-brachytherapy value.' .....	42
Table 3: Patient 2's individual data. Each statistic is written in the format of 'Pre-EBRT value, Pre-brachytherapy value.' .....	42
Table 4: Patient 3's individual data. Each statistic is written in the format of 'Pre-EBRT value, Pre-brachytherapy value.' .....	42
Table 5: Patient 4's individual data. Each statistic is written in the format of 'Pre-EBRT value, Pre-brachytherapy value.' .....	43
Table 6: Patient 5's individual data. Each statistic is written in the format of 'Pre-EBRT value, Pre-brachytherapy value.' .....	43
Table 7: Patient 6's individual data. Each statistic is written in the format of 'Pre-EBRT value, Pre-brachytherapy value.' .....	43
Table 8: Average statistics of all patients for GTV contoured with axial T2 MRI, with the help of DWI, and with the help of ADC.....	44
Table 9: Mean pixel values within the CTV <sub>HR</sub> , CTV <sub>HR</sub> -Tandem, and CTV <sub>HR</sub> -Tandem expansion on each b-value DW image.....	46

## List of Figures

Figure 1: Schematic of a cervical cancer case and the associated GTV, CTV <sub>HR</sub> , and CTV <sub>IR</sub> (Haie-Meder et al, 2003). .....	10
Figure 2: Clinical treatment workflow for gynecological malignancies. ....	12
Figure 3: Fractionation and imaging schemes for GYN patients. ....	13
Figure 4: Schematic of Jaccard index (left) and Dice coefficient (right) calculation. ....	22
Figure 5: MIM workflow for GTV contouring .....	23
Figure 6: Photos of the ice-water phantom experiment set-up. a) geometry; b) with ice water content on MR scanner table. ....	25
Figure 7: Pixel values of MATLAB-derived DW image (cDWI1000) plotted against DW image from console (mDWI1000), both at $b=1000\text{s/mm}^2$ . ....	28
Figure 8: Pixel-wise difference histogram for MATLAB-derived and console-derived ADC maps at $b=0,1000\text{s/mm}^2$ . ....	29
Figure 9: Visual comparison of the MATLAB-derived and console-derived ADC maps at $b=0, 1000\text{s/mm}^2$ . ....	29
Figure 10: Example a) tumor (red), b) endometrium (yellow), myometrium (blue), c) endocervical canal (pink), and d) gluteal subcutaneous fat (orange) ROIs .....	31
Figure 11: Contrast to noise ratios of each ROI compared to tumor at $b=1000, 1300, 1600, 1800, \text{ and } 2000 \text{ s/mm}^2$ . Plot is for pre-EBRT and pre-BT values averaged together .....	31
Figure 12: a) Example pre-EBRT images for Patient 1, b) and the corresponding pre-BT images. The field of view is cropped to show relevant structures. ....	32
Figure 13: a) Example pre-EBRT images for Patient 2, b) and the corresponding pre-BT images. The field of view is cropped to show relevant structures .....	33
Figure 14: a) Example pre-EBRT images for Patient 3, b) and the corresponding pre-BT images. The field of view is cropped to show relevant structures .....	34
Figure 15: a) Example pre-EBRT images for Patient 4, b) and the corresponding pre-BT images. The field of view is cropped to show relevant structures .....	35

Figure 16: Example pre-EBRT images for Patient 5, b) and the corresponding pre-BT images. The field of view is cropped to show relevant structures .....	36
Figure 17: Average rankings of total image quality and tumor conspicuity, with values closer to 1 representing better conspicuity and better overall image quality.....	38
Figure 18: Example slice from Patient 1's a) pre-EBRT scan and b) pre-brachytherapy scan with the overlaid GTVs.....	40
Figure 19: The CTV <sub>HR</sub> , CTV <sub>HR</sub> -Tandem, CTV <sub>HR</sub> -Tandem expansion overlaid on a DW image slice at various b-value.....	45
Figure 20: Example slice from ice water experiment of a) axial T2 MRI, b) DWI, and c) ADC map. The tandem is contoured on each image. ....	46
Figure 21: Example CTV <sub>HR</sub> contour (left) and CTV <sub>HR</sub> -tandem contour (right).....	48
Figure 22: Box and whisker plot of the mean pixel values within each CTV <sub>HR</sub> -tandem on the DW image set.....	49
Figure 23: Box and whisker plot of the mean pixel values within each CTV <sub>HR</sub> -tandem on the ADC maps.....	49
Figure 24: Box and whisker plot of the standard deviation of the pixel values within each CTV <sub>HR</sub> -tandem on the DW image set. ....	50
Figure 25: Box and whisker plot of the standard deviation of the pixel values within each CTV <sub>HR</sub> -tandem on the ADC maps. ....	50
Figure 26: a) Patient mean pixel values on DWI, b) standard deviations on DWI, c) mean pixel values on ADC, d) and standard deviations on ADC throughout BT.....	51

## **Acknowledgements**

I would like to express my sincere gratitude to my research advisor, Dr. Oana Craciunescu, for her unwavering support throughout my time at Duke University. Also, I would like to thank Dr. Yongbok Kim for his insightful comments and help along the way. I also thank Dr. Chunhao Wang for his coding insight and helpful lines of thinking. Further, I extend my thanks to Dr. Scott Robertson for his technical support and enthusiasm for the project. Last but not least, I extend my never-ending thanks to Dr. Junzo Chino and Dr. Diandra Ayala-Peacock for their patience and clinical guidance

# **1. Introduction**

## ***1.1 Gynecological Cancer and the Role of Radiation Therapy***

In 2023, an estimated 114,810 people were diagnosed with gynecological (GYN) cancer annually (Foundation for Women's Cancer, 2024), with the five main types being cervical, ovarian, uterine, vaginal, and vulvar cancer (Centers for Disease Control and Prevention, 2019). Uterine and cervical cancer, accounting for 75,050 new cases each year, are primarily treated with radiation therapy (American Society for Radiation Oncology, 2020). Despite being preventable through screening, cervical cancer is the second leading cause of cancer death in women 20 to 39 years of age and is the second most common and third deadliest form of cancer for women worldwide (Siegel et al, 2021; Williamson et al, 2021). Standard treatment for GYN malignancies includes a mix of chemotherapy, radiation, and surgery (Centers for Disease Control and Prevention, 2023). The standard treatment for locally advanced cervical cancer is external beam radiation therapy (EBRT) with concurrent chemotherapy followed by a brachytherapy boost.

### **1.1.1 Role of EBRT**

EBRT uses a beam of ionizing radiation outside the body to damage cancer cells, and the role of radiation therapy depends on cancer type, stage, location, and patient's health. It aims to cure, control growth, or alleviate symptoms. EBRT is typically

administered daily, Monday through Friday, over a span of five to six weeks. The three types of EBRT include three-dimensional conformal radiotherapy (3D-CRT), intensity-modulated radiation therapy (IMRT), and volumetric modulated arc therapy (VMAT). 3D-CRT utilizes three-dimensional CT scans to manually optimize the target dose while sparing OARs. IMRT uses inverse planning to modulate beam intensities to a desired dose distribution, maximizing the target dose and sparing OARs (Bakiu et al, 2013). VMAT rotates the linear accelerator around the patient while using modulated radiation beams for precise dose delivery (Quan et al, 2012). Either IMRT or VMAT can be used for GYN malignancies depending on the location and spread of the tumor. Additionally, the simultaneous integrated boost (SIB) technique in IMRT or VMAT allows the delivery of varying doses to distinct target volumes in a single treatment fraction. Studies comparing SIB IMRT to sequential IMRT or SIB VMAT found comparable target coverage, reduced hot spots, improved OAR sparing, and a reduction in treatment times compared to sequential IMRT (Feng et al, 2016; Vergalaso et al, 2017).

### **1.1.2 Role of Brachytherapy**

Internal radiation therapy, also known as brachytherapy, utilizes sealed radioactive sources to deliver a high dose to the target while sparing organs at risk (OARs). This is a favorable approach in GYN malignancies due to treatment target accessibility and rapid dose fall-off in nearby tissues like the bladder and rectum. Despite a significant decline in its utilization for cervical cancer cases in the United States between 1988 and 2009, it has been found to be independently associated with a

significantly higher cause-specific and overall survival (Han et al, 2013). Additionally, image-guided brachytherapy has been shown to reduce morbidity (Pötter et al, 2021), highlighting its importance. Treatment components for GYN cancer include the intrauterine applicator (tandem) and intravaginal components such as vaginal ovoids or a vaginal ring. Intracavitary brachytherapy, combining tandem with ovoids/ring, is frequently used for locally advanced cervical cancer. However, this technique's dosing relies on a reference point without considering the size and shape of the target volume, proving inadequate for large and/or irregular tumors. The use of image-guided adaptive brachytherapy with a hybrid intracavitary and interstitial technique shows promise in improving clinical outcomes. For example, one institution found that hybrid brachytherapy could provide better local control and acceptable late toxicity profiles for locally advanced cervical cancer patients (Murakami et al, 2019). Additionally, simulation study found that high-risk clinical target volumes ( $CTV_{HRS}$ ) larger than 4cm x 3cm x 3cm are better treated using the hybrid approach rather than intracavitary alone (Yoshida et al, 2015). In the era of precision medicine, personalized treatment plans should thoroughly evaluate target volumes and OARs to optimize patient outcomes.

#### **1.1.2.1 High-Dose Rate (HDR) Brachytherapy**

HDR brachytherapy employs a dose rate of  $\geq 12\text{Gy/h}$  and utilizes remote afterloading due to its high source activity. The most common radionuclide used for HDR brachytherapy is iridium-192 (Harkenrider et al, 2021). Typically delivered in three to six fractions once or twice weekly, HDR GYN brachytherapy is commonly used for cervical

cancer treatment and is also applicable to early-stage uterine cancer (American Society for Radiation Oncology, 2020). Viani et al recommends using HDR brachytherapy for all cervical cancer cases, as opposed to low-dose rate (LDR) brachytherapy. Further, HDR brachytherapy has been shown to be beneficial in the palliation of bleeding from cervical carcinoma (Grigsby et al, 2002). A major advantage of HDR over LDR brachytherapy is the short treatment times, allowing treatment to occur on an outpatient basis. However, these short treatment times do not allow for much error correction, so personnel must be properly trained and constantly alert (Nag, 2004).

#### **1.1.2.2 Low-Dose Rate (LDR) Brachytherapy**

The dose rates of LDR brachytherapy range between 4 and 200 cGy/h, with source loading being either manual or automatic. Sources used throughout LDR brachytherapy's history include radium-226, cesium-137, iridium-192, iodine-125, and palladium-103 (Woodhouse et al, 2022). A common application of LDR brachytherapy is in the treatment of prostate cancer because it has shown advantages over HDR brachytherapy regarding relapse rates and serious adverse event profiles (BXTA, 2023). Looking specifically at cervical cancer, Mai et al attempted to replicate the classical LDR pear-shaped dose distribution in HDR using various dose specification methods and found that prescribing dose to tapered points along the tandem and ovoid surfaces gave the best results. Overall, LDR brachytherapy has more data behind it compared to HDR, but it occurs on an inpatient basis and increases radiation exposure to staff (Stewart &

Viswanathan, 2006). It is important to consider whether LDR or HDR brachytherapy is more appropriate for treatment on a patient-by-patient basis.

## ***1.2 The Role of Imaging in Gynecological Malignancies***

### **1.2.1 CT, PET, MRI**

Various imaging modalities are employed in clinical settings to assess gynecological malignancies, including computed tomography (CT), positron emission tomography (PET), and magnetic resonance imaging (MRI). CT scanning utilizes x-ray images captured at various angles around the body to construct a three-dimensional rendering (Mayo Foundation for Medical Education and Research, 2022). PET scanning involves the administration of a radioactive tracer to reveal metabolic or biochemical function within tissues. It is often combined with CT or MRI, offering early detection capabilities for certain diseases (Mayo Foundation for Medical Education and Research, 2023). MRI is often used for clinical diagnosis, relying on the behavior of mobile protons, primarily in water. T1- and T2-weighted MR images provide differences in the contrast of various tissues through the leverage of specific radiofrequency pulse sequences to manipulate proton spin transitions within a uniform magnetic field. When the body is placed within a uniform magnetic field ( $B_0$ ), the net magnetic moment of the nuclei in the body align parallel or antiparallel with  $B_0$ . The longitudinal or T1 relaxation time refers to the period for 63% of the net z-magnetization to return to equilibrium when altered. Further, the transverse components of the magnetization vector for the nuclei in

the body precess about  $B_0$  at a specific frequency. However, each tissue experiences local field inhomogeneities that cause the nuclei to lose coherence in their precession, known as transverse or T2 relaxation time. These relaxation times vary between tissues, contributing to image contrast in MRI.

In MR image acquisition, radiofrequency pulses are applied in a specific pulse sequence (Smith, 2012). Two important acquisition parameters derived from these pulse sequences include the time of repetition (TR) and the time of echo (TE), where TR is the repetition time for the sequence and TE is the time to the maximum echo amplitude. Tailoring acquisition parameters, such as TE and TR, facilitates accurate target delineation in patients with gynecological malignancies (Pickens, 2012).

### **1.2.2 DWI/ADC Applications in Radiation Therapy**

Diffusion-weighted image (DWI) acquisition and apparent diffusion coefficient (ADC) map calculation is detailed in Section 2.3 in Methods. DW-MRI and its derived ADC maps play a significant role in radiation oncology, particularly for cervical cancer patients (Ho et al, 2017; Rosa et al, 2020; Kumar et al, 2020; Dappa et al, 2017). Tumors typically exhibit lower ADC values compared to normal tissue due to limited diffusion (Haack et al, 2010). Ho et al. demonstrated the prognostic value of mean ADC values from pretreatment MRI in predicting disease-free survival (DFS) in cervical patients, independent of clinical factors. However, this study focused on a single ADC parameter in a two-dimensional volume.

In radiomics research, Zhou et al. explored various features to predict DFS in early-stage squamous cervical cancer, identifying independent predictors of recurrence. However, 32 of their 191 patients underwent additional chemotherapy, possibly skewing results. Another study constructed a radiomic signature (RS) consisting of one T2-weighted and three ADC parameters, showing its superiority in predicting DFS compared to clinical models (Liu et al, 2009). Tamai et al. and Naganawa et al. found the mean ADC of uterine sarcomas and cervical cancer lesions to be significantly lower than that of normal tissue. Furthermore, significantly lower ADC values were found in malignant lesions of the endometrial cavity compared to benign lesions (Fujii et al, 2008). These findings support the notion that tumors have reduced diffusion rates.

Haack et al. investigated ADC values within GEC-ESTRO target volumes of locally advanced cervical cancer patients and found the mean ADC in the GTV at the time of brachytherapy ( $GTV_{BT}$ ) to be greater than that of the  $CTV_{HR}$ , which in turn was greater than that of the IR-CTV. This substantiates the claim that the tumor volume ( $GTV_{BT}$ ) is that with the lowest diffusion. They also found no significant change in the ADC level and the volume with  $ADC < 1.2 \times 10^{-3} \text{ mm}^2/\text{s}$  ( $ADC_{low}$ ) from the first and second brachytherapy fractions, corroborating that changes in ADC level and volumes are stable at the time of brachytherapy. In the context of treatment outcomes, Gladwish et al. highlighted the prognostic significance  $ADC_{95}$  in women with locally advanced cervical cancer.

Studies have investigated optimal b-values in gynecological malignancies. For example, Moribata et al. explored a variety of b-values from 1000 to 2000 s/mm<sup>2</sup> using computed DWI. Their qualitative analysis involved two radiologists scoring the image quality of DW images at various b-values with reference to the DW image at b=1000 s/mm<sup>2</sup>. Further, their quantitative analysis analyzed the contrast ratios of the tumor to different ROIs. They found that b-values 1300 and 1600 s/mm<sup>2</sup> gave the best tumor conspicuity and overall image quality in cervical cancer patients. Kuang et al. assessed the impact of difference b-values, specifically b=0, 600 s/mm<sup>2</sup> and b=0, 1000 s/mm<sup>2</sup>, in evaluating treatment response to radiochemotherapy in 75 cervical cancer patients. They concluded that ADC maps calculated at b=0, 1000 s/mm<sup>2</sup> were more reliable for assessing treatment response compared to b=0, 600 s/mm<sup>2</sup>.

### ***1.3 Artifacts in MRI Images Acquired for Brachytherapy***

While MRI is highly valuable for tumor staging, treatment planning, and treatment response tracking, it is susceptible to imaging artifacts, particularly concerning titanium brachytherapy applicators and needles. When placed in a magnetic field, materials like titanium induce magnetization proportional to their magnetic susceptibility and the field strength, where  $M$  is the induced magnetization,  $c$  is the magnetic susceptibility, and  $H$  is the magnetic field strength (Equation 1). This induced magnetization alters the initial magnetic field, leading to distortions that manifest as image artifacts, affecting signal intensity.

$$M=\chi H \quad (1)$$

Concerns about using DWI at 3T with titanium applicators have been raised due to susceptibility artifacts and geometric distortions (Soliman et al, 2016). Søren et al explored geometrical distortion correction techniques for DW-MRI and ADC in brachytherapy for locally advanced cervical cancer. While deformable image registration (DIR) was better than  $B_0$  field mapping in correcting for geometrical distortions, residual uncertainties persisted using both techniques. Interestingly, no significant differences were observed in ADC values with or without corrections.

The potential of MRI and DWI in gynecological malignancies makes artifact characterization even more pertinent. For example, utilizing MRI for residual tumor volume contouring before each radiotherapy fraction has demonstrated potential in improving cervical cancer outcomes (Tanderup et al, 2014). The choice of magnet and sequences impacts artifact presence in DW images from brachytherapy applicators, necessitating further characterization.

#### ***1.4 Clinical Radiation Therapy Treatment Workflow for GYN***

The clinical workflow for gynecological malignancies begins with CT simulation, which is used to replicate patient positioning during treatment. Next, target volumes and OARs are delineated using CT with MRI or PET assistance for EBRT and T2-weighted MRI for brachytherapy. These contours form the basis for dose calculation, crucial for

maximizing tumor control and sparing normal tissue. GEC-ESTRO defines the gross tumor volume at diagnosis ( $GTV_D$ ) as the “macroscopic tumor extension at diagnosis as detected by clinical examination (visualization and palpation) and as visualized on MRI...” Similarly, the gross tumor volume at the time of brachytherapy ( $GTV_B$ ) is the “macroscopic tumor extension at time of BT as detected by clinical examination and as visualized on MRI...” The high-risk CTV for BT ( $CTV_{HR}$ ) includes the  $GTV_B$ , whole cervix, and presumed extracervical tumor extension. Finally, the intermediate risk CTV for BT ( $CTV_{IR}$ ) includes the  $CTV_{HR}$  with a 5-15mm margin (Haie-Meder et al, 2004). A schematic of a cervical cancer case and the associated  $GTV$ ,  $CTV_{HR}$ , and  $CTV_{IR}$  can be seen in Figure 1. Once contours are completed, dose constraints are met, and the treatment plan is optimized, treatment can begin. However, pelvic organs are commonly displaced or undergo volumetric changes, so image guidance aids in visualizing daily target and OAR positioning. For example, image-guided brachytherapy has been shown to improve local control and reduce toxicity compared to point-based dose planning (Williamson et al, 2021).

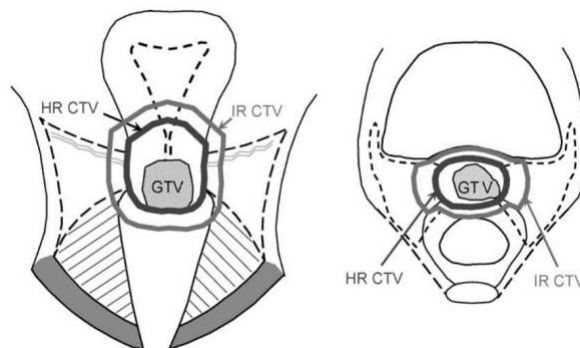


**Figure 1: Schematic of a cervical cancer case and the associated  $GTV$ ,  $CTV_{HR}$ , and  $CTV_{IR}$  (Haie-Meder et al, 2003).**

For gynecological malignancies, the following steps occur from diagnosis to treatment: 1) consultation; 2) CT simulation; 3) target and OAR delineation; 4) treatment planning; 5) plan check and quality assurance (QA); 6) patient setup; and 7) treatment delivery. EBRT follows a fractionated schedule spanning five weeks, with daily kV images and weekly cone-beam computed tomography (CBCT) for setup confirmation. A flowchart of the clinical workflow and fractionation/imaging scheme can be seen in Figure 2. The most common EBRT fractionation scheme is 25 fractions at 1.8Gy per fraction. High-dose rate (HDR) brachytherapy follows EBRT, typically delivered in five fractions over two weeks at 5.5 or 6Gy per fraction, depending on tumor extent after EBRT (Viswanathan et al, 2012). At Duke, MRI acquisitions, including DWI images, are performed at various time points during treatment, as depicted in Figure 3.

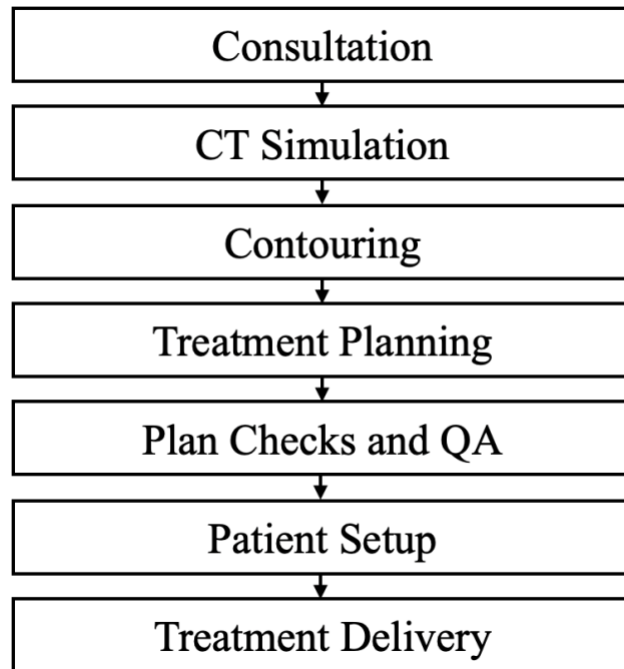


Figure 2: Clinical treatment workflow for gynecological malignancies.

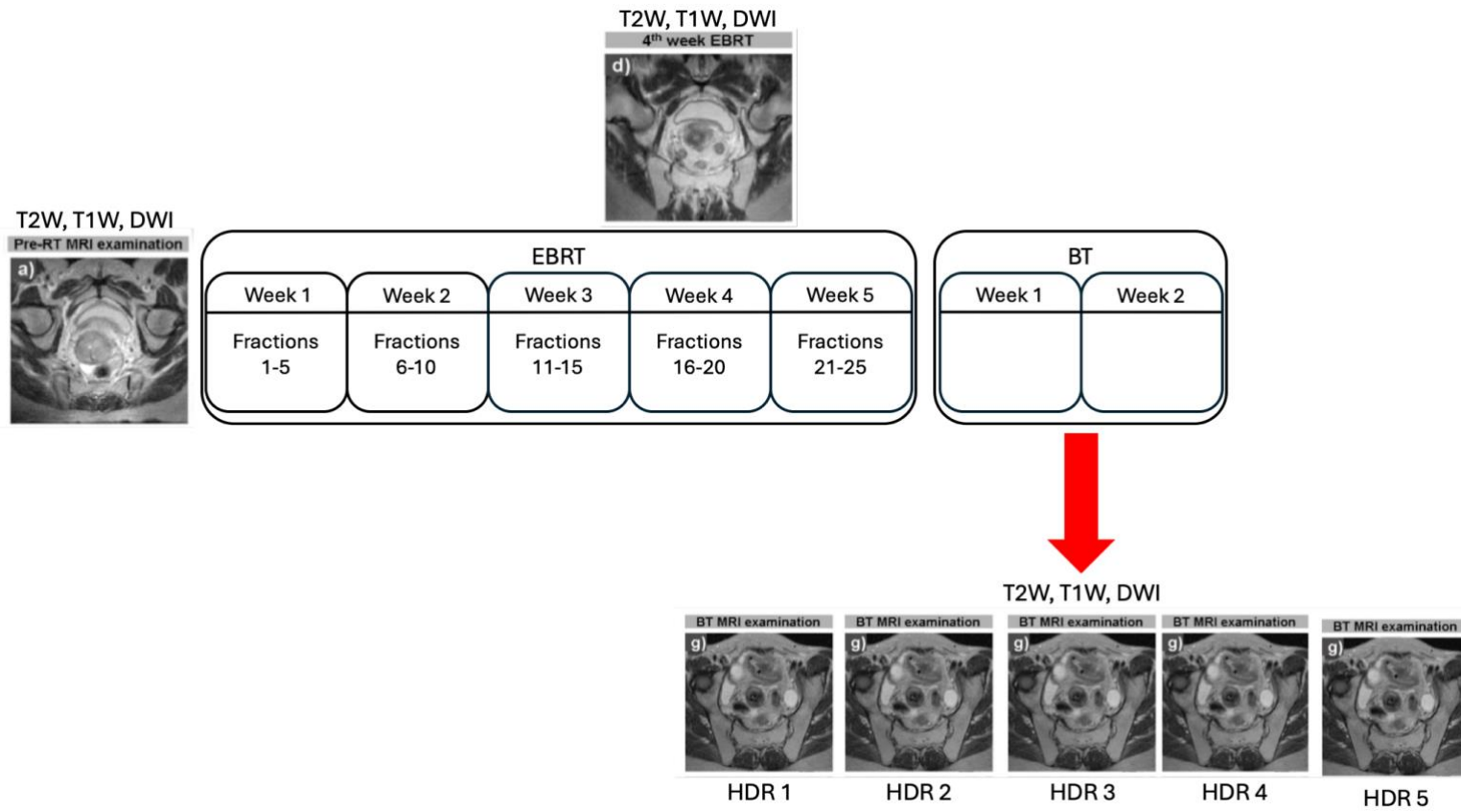


Figure 3: Fractionation and imaging schemes for GYN patients.

## ***1.5 Purpose***

The purpose of this thesis is twofold: 1) to validate and optimize DW imaging for GYN applications, and 2) to evaluate the potential clinical applications of DW imaging in the management of gynecological cancer patients undergoing EBRT and HDR brachytherapy. DW images and ADC maps have shown promise in diagnostic imaging and disease-free survival prediction in various sites (Bruegel et al, 2008; Fujii et al, 2008; Gladwish et al, 2016; Guo et al, 2002; Haider et al, 2007; Tamai et al, 2008). However, analysis using multiple time points throughout treatment does not appear in the literature to the best of our knowledge. Thus, this study aims to accomplish its goals in two main parts.

In the first part, DW-MRI optimization in GYN cancer patients undergoing EBRT and brachytherapy is performed. This involves validating MR console-generated DWI and ADC maps using an in-house MATLAB code. This was done by calculating correlation coefficients between the console-generated and Matlab-generated image set. Linearity was also checked between the console-generated and Matlab-generated sets' pixel values for the DWI set, and a pixel-wise difference histogram was used for further verification of the ADC maps. After image set validation, b-value optimization was accomplished through a quantitative analysis of different contrast-to-noise ratios (CNRs) and a qualitative analysis involving two physician's ranking tumor conspicuity and total image quality for different b-value sets.

In the second part of this study, after optimizing the b-value, the role of DWI/ADC maps in GTV contouring before and after EBRT was investigated. Currently, GTVs are delineated using T2 MRI, providing only anatomical information. The addition of physiological information from functional imaging aims to enhance current clinical contouring workflows. Our hypothesis is that the GTVs contoured with the assistance of DWI and ADC will be smaller than those contoured without DWI and ADC due to functional imaging elucidating more disease-ridden areas. Clinically, physicians could boost the dose to these areas.

The final component of this study analyzed CTV<sub>HR</sub> changes throughout the course of brachytherapy. This was accomplished by overlaying the treatment-approved CTV<sub>HR</sub> on the ax-T2 MRI, DW image set, and ADC map and analyzing the pixel differences. Overall, this study aims to further validate and optimize DW imaging for GYN applications and elucidate the clinical role of DWI in the management of gynecological cancer patients undergoing EBRT and HDR brachytherapy.

## 2. Materials and Methods

### *2.1 MRI Parameters, Patient Selection, and Patient Treatment*

In this retrospective study, female patients diagnosed with different gynecological malignancies were enrolled under an Institutional Review Board (IRB) approved protocol. The treatment regimen involved five weeks of EBRT followed by five fractions of brachytherapy (BT) administered over a two-week period. Imaging data, including axial T1-weighted MR images, axial T2-weighted MR images, and diffusion-weighted images, were acquired at three key time points: prior to EBRT (pre-EBRT), during the fourth week of EBRT (pre-BT), and following each fraction of BT (HDR1-5). The pre-BT scan aimed to delineate any residual tumor volume remaining post-EBRT delivery, crucial for subsequent brachytherapy planning. Brachytherapy treatment was delivered using either a tandem and ovoids or a vaginal cylinder. Imaging was performed using a Siemens Magnetom Skyra 3.0T scanner, and the parameters for the acquired imaging sequences were as follows:

**Localizer:** FOV=430mm, spatial resolution=256mm, slice thickness=1.7x1.7x6.0mm, TR=1400ms, TE=94ms

**Axial T1:** FOV=200mm, spatial resolution=0.9x0.9x1.0mm, slice thickness=1.0mm, TR=3.7ms, TE=1.33ms

**Axial T2:** FOV=320mm, spatial resolution=0.9x0.9x3.0mm, slice thickness=3.00mm, TR=2000ms, TE=121ms

**Trace (DWI):** FOV=300mm, resolution=1.3x1.3x3.0mm, slice thickness=3.0mm,  
 TR=11220ms, TE1=73ms, TE2=121ms, b-values=0,1000 (s/mm<sup>2</sup>)

## ***2.2 Diffusion-Weighted Magnetic Resonance Imaging (DW-MRI)***

DW-MRI is a functional MRI modality that examines the microstructure of tissues through an MR imaging sequence that detects the Brownian motion of water molecules (Arlinghaus & Yankeelov, 2012). Water molecules do not move freely in tissue; they encounter tissue microstructures that limit their average diffusion displacement, defined by their apparent diffusion coefficient (ADC). Some characteristics of tissue that impact the ADC are cellularity, extracellular volume fraction (ECVF), membrane permeability, and tortuosity.

The Bloch equation provides a description of spin magnetization in a strong magnetic field (Equation 2), where  $M = (M_x, M_y, M_z)^T$  is the local magnetization,  $M_0$  is the equilibrium magnetization,  $B$  is the static scanner field,  $T_1$  is the transverse relaxation constant,  $T_2$  is the longitudinal relaxation constant,  $\gamma$  is the gyromagnetic constant, and  $i$ ,  $j$ , and  $k$  are unit vectors for the cardinal directions.

$$\frac{dM}{dt} = \gamma M \times B - \frac{M_x i + M_y j}{T_2} - \frac{M_z - M_0}{T_1} k$$

(2)

This equation does not consider diffusion's effects on spin magnetization. Thus, Torrey incorporated an additional diffusion term (Equation 3), and recent literature has further altered this equation to include a linear flow term defined by the vector  $u$

(Equation 4). The quantification of the diffusive term in the Bloch-Torrey equation through the use of different pulse sequences has led to diffusion-weighted MRI (Hall, 2016).

$$\frac{dM}{dt} = \gamma M \times B - \frac{M_x i + M_y j}{T_2} - \frac{M_z - M_0}{T_1} k - \nabla \cdot (D \nabla M) \quad (3)$$

$$\frac{dM}{dt} = \gamma M \times B - \frac{M_x i + M_y j}{T_2} - \frac{M_z - M_0}{T_1} k - \nabla \cdot (D \nabla M) - \nabla \cdot u M$$

(4)

After neglecting relaxation effects, Stejskal and Tanner used the solution Bloch-Torrey equation for pulsed gradient spin echo sequences to characterize diffusion-weighted signal attenuation. They found that the signal at a specific b-value, which describes the sensitivity of the imaging sequence to diffusion, depends on the signal at a lower b-value (i.e. b=0 s/mm<sup>2</sup>), the ADC, and the b-value (Equation 5). The b-value is defined where  $\delta$  is the duration,  $\Delta$  is the time separation between gradient pulses, and  $g$  is the amplitude of the diffusion sensitizing gradient pulse (Equation 6) (Ozcan et al, 2012).

$$S_b = S_0 \exp(-b \times ADC) \quad (5)$$

$$b = \gamma^2 \delta^2 (\Delta - \frac{1}{3}\delta) g^2 \quad (6)$$

Equation 5 assumes a monoexponential model between the signal and the diffusion coefficient, which may oversimplify the complex tissue environments within the body. Other models that have been explored in the literature are a multiexponential model and a stretched exponential model. However, a monoexponential model is valid to assume in most cancer cases. The b-value in Equation 1 must be optimized before a DW-MRI study, and the optimal b-value is dependent on things such as the tissue of interest's

degree of anisotropy and ADC, the amount of perfusion in the tissue, and the background noise. DWI and ADC maps have shown potential in tumor detection and characterization in various sites, such as the prostate (Haider et al, 2007), liver (Bruegel et al, 2008), and breast (Guo et al, 2002).

### ***2.3 DW Image and ADC Map Validation***

Prior to retrospective analysis, an in-house MATLAB code was used to validate the DW image and ADC map calculations performed at the MR console. This validation aimed to ensure accurate calculation of DW images at various b-values and the proper generation of ADC maps. To verify DW image calculation, correlation coefficients were computed between two DW image sets for each slice: the DW image set acquired during the scan at  $b=1000 \text{ s/mm}^2$  and the DW image set calculated retrospectively on the MR console at the same b-value. Additionally, linearity was assessed by comparing the pixel values of the acquired set with those of the calculated set in ROIs of tumor, endocervical canal, endometrium, myometrium, and gluteal subcutaneous fat. For verifying ADC map calculation at the MR console at  $b=0,1000 \text{ s/mm}^2$ , an in-house MATLAB code was used to retrospectively calculate the ADC map using the DW  $b=0$  and  $b=1000 \text{ s/mm}^2$  images from console. Subsequently, the correlation coefficients between the MATLAB-derived and console-derived ADC map were analyzed for comparison.

## ***2.4 Optimization of b-Value***

Methods from Moribata et al. were incorporated in this study, which conducted b-value optimization through quantitative and qualitative analyses. While their study focused solely on pre-EBRT data, we included both pre-EBRT and pre-BT data. Also, while they examined contrast ratios, we investigated contrast-to-noise ratios. Our aim was to confirm their findings for our smaller patient cohort while expanding on their time points and statistical methods.

For the quantitative analysis, representative sections of tumor, endocervical canal, endometrium, myometrium, and gluteal subcutaneous fat were delineated on two slices of pre-EBRT and pre-BT axial T2 MR scans for five patients. Subsequently, DW images were retrospectively generated at various b-values (1000, 1300, 1600, 1800, and 2000  $\text{s/mm}^2$ ), and contrast-to-noise ratios (CNRs) were computed on these images. The CNRs were calculated by determining the absolute value of the difference between mean pixel values of the tumor and ROI, divided by the sum of their mean pixel values, normalized by a noise measurement (Equation 2). Noise measurements were obtained by computing standard deviation within an ROI in air outside the body. The tumor and various ROIs were delineated as large as feasible while ensuring their reliability. Additionally, average tumor and fat signal loss between DWI sequences at  $b=1000$  and  $b=2000$   $\text{s/mm}^2$  were determined to aid in b-value optimization. The tumor and fat signal loss were calculated using Equation 3.

$$CNR = \frac{|Tumor\ Mean\ Pixel\ Value - ROI\ Mean\ Pixel\ Value|}{Tumor\ Mean\ Pixel\ Value + ROI\ Mean\ Pixel\ Value} \div Noise \quad (2)$$

$$Signal\ Loss(\%) = \left( \frac{(Signal\ at\ b=1000s/mm^2) - (Signal\ at\ b=2000s/mm^2)}{(Signal\ at\ b=1000s/mm^2)} \right) \times 100 \quad (3)$$

Qualitatively, axial DWI sets of five patients before EBRT and BT, at b-values of 1000, 1300, 1600, 1800, and 2000 s/mm<sup>2</sup>, were reviewed by two radiation oncologists. They ranked the images based on tumor conspicuity and overall image quality on a scale of 1-5, with 1 representing the highest quality and 5 the worst. The average rankings were then utilized alongside quantitative analysis to determine the optimal b-value for subsequent phases of this study.

## ***2.5 Gross Tumor Volume (GTV) Analysis***

After determining the optimal b-value (b=1300 s/mm<sup>2</sup>), a Medical Image Merge (MIM Software, 2003) workflow was established for GTV contour analysis (Figure 5). This workflow guided a radiation oncologist in delineating GTVs on three image sets; axial T2 MRI (GTV<sub>T2W</sub>), axial T2 MRI fused with DWI at b=1300 s/mm<sup>2</sup> (GTV<sub>DWI</sub>), and axial T2 MRI fused with ADC at b=0, 1000 s/mm<sup>2</sup> (GTV<sub>ADC</sub>). The b-value chosen for ADC map calculation was b=0, 1000 s/mm<sup>2</sup> because ADC theoretically does not change with b-value.

Metrics calculated using MIM included the volume of each GTV, Dice coefficient, Hausdorff distance, and Jaccard index of each GTV compared to GTV<sub>T2W</sub>, as well as the mean and maximum pixel values within the GTV. Given Contours A and B,

the Hausdorff distance is defined as the greatest of all distances from one point on contour A to the closest point on contour B, indicating contour dissimilarity. The Dice coefficient measures pixel similarity between two contours, ranging from 0 to 1, with 1 indicating identical contours. The Jaccard index quantifies the degree of overlap between two contours, with 1 representing complete overlap and 0 no overlap. Visual aids for calculating the Jaccard index (Unitech, 2020) and Dice coefficient (Amine, 2021) are shown in Figure 4. Differences in these metrics were compared using a Wilcoxon signed-rank test, a non-parametric statistical test for comparing two dependent samples (McClenaghan, 2023).

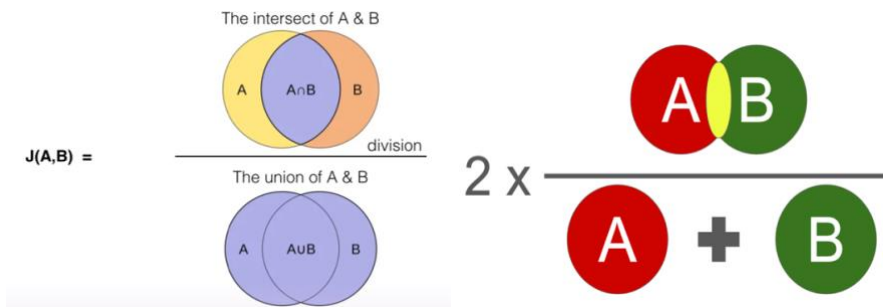


**Figure 4: Schematic of Jaccard index (left) and Dice coefficient (right) calculation.**

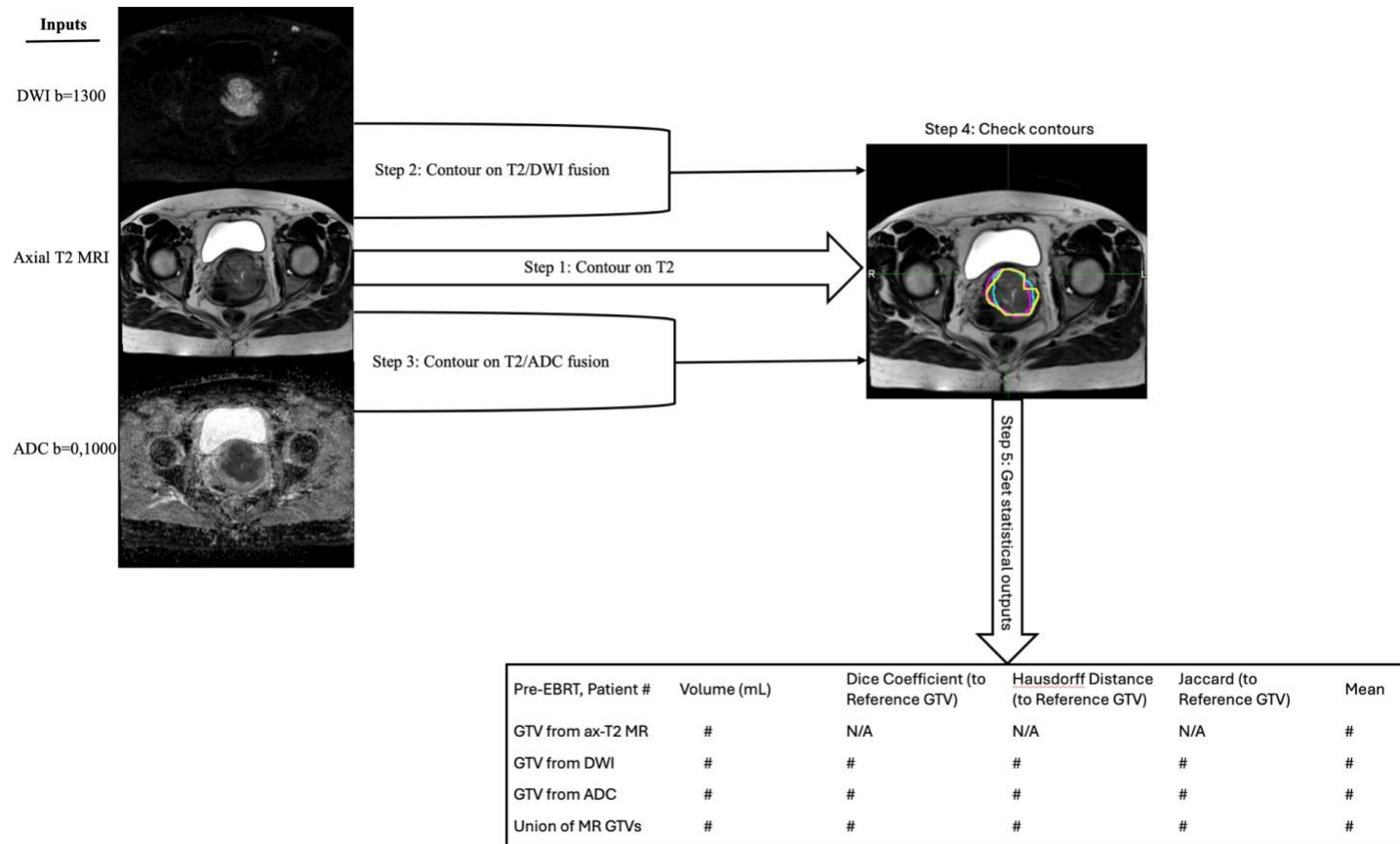


**Figure 5: MIM workflow for GTV contouring.**

## ***2.6 Applicator Artifact Quantification***

If a tandem and ovoids were utilized for a patient in this study, it was necessary to address artifacts arising from the titanium applicator. A preliminary quantitative analysis was conducted on a single patient. DW images were generated at  $b=1000, 1100, 1300, 1500, 1800, \text{ and } 2000 \text{ s/mm}^2$ . A representative slice in the middle of the  $\text{CTV}_{\text{HR}}$  was chosen, and the mean pixel value within this slice was calculated for all b-value images. The tandem was contoured and subtracted from the  $\text{CTV}_{\text{HR}}$  ( $\text{CTV}_{\text{HR-tandem}}$ ), and the mean pixel value was calculated for the  $\text{CTV}_{\text{HR-tandem}}$  on the same slice for each b-value image. A 3mm margin was added to the tandem, and the mean pixel value within the  $\text{CTV}_{\text{HR}}$  expansion ( $\text{CTV}_{\text{HR-tandem expansion}}$ ) was calculated on that same slice for all b-value images. Differences between these mean pixel values were analyzed to assess the validity of using the  $\text{CTV}_{\text{HR-tandem}}$  in the longitudinal analysis of this study.

Furthermore, an experiment was conducted in an ice water phantom following a methodology similar to that proposed in a previous study (Chenevert et al, 2011). This approach was chosen as a reference due to its promising outcomes and the availability of cost-effective materials. Within the ice water phantom, a tandem was inserted into a butternut squash and imaged using the same MR parameters as outlined earlier. The resulting images were visually inspected for any notable artifacts occurring outside of the tandem. Figure 6 illustrates the experimental setup of the ice water phantom used for artifact quantification that includes a 30 degree Ti tandem, 6cm length, and 2 ovoids with mini caps.

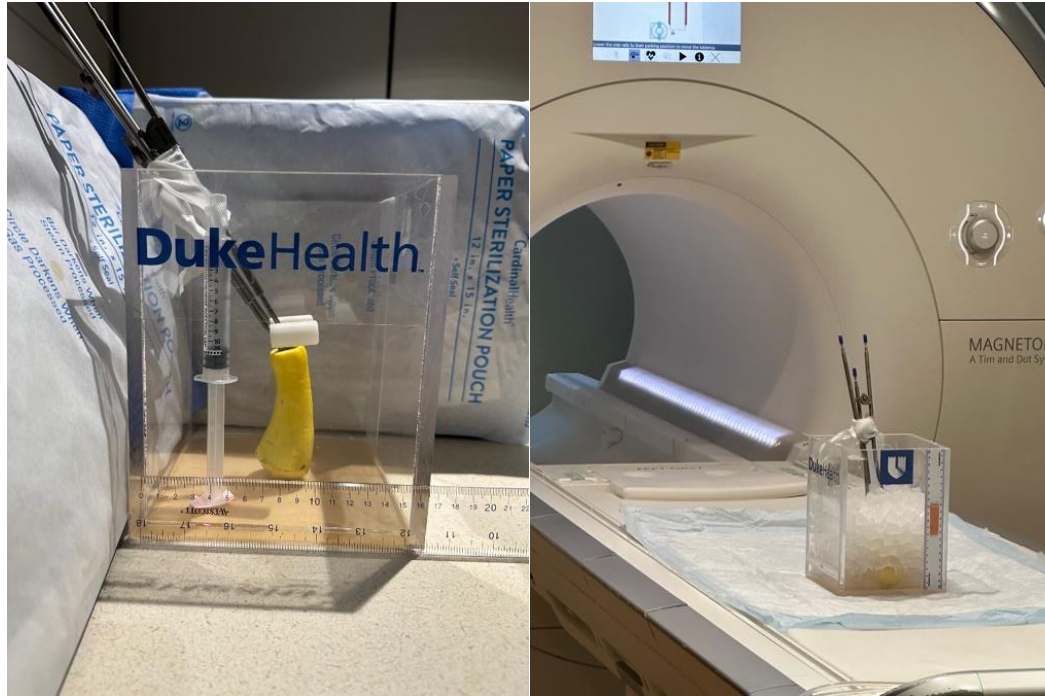


**Figure 6: Photos of the ice-water phantom experiment set-up. a) geometry; b) with ice water content on MR scanner table.**

## ***2.7 Longitudinal Analysis of $CTV_{HRS}$***

The longitudinal analysis aimed to examine pixel value changes within the  $CTV_{HRS}$  utilized for treatment across axial T2 MRIs, DW images, and ADC maps. This analysis was conducted using MIM software and data from 14 patients. For each HDR brachytherapy fraction with a corresponding diffusion-weighted scan, the  $CTV_{HR}$  was overlaid on the axial T2 MRI set, the DWI set, and the ADC maps after subtracting the tandem contour ( $CTV_{HR}$ -tandem). The pixel values within each overlaid  $CTV_{HR}$ -tandem were evaluated by assessing the mean and standard deviation. These values were averaged for each patient's corresponding fraction to examine changes in the  $CTV_{HR}$ -tandem throughout brachytherapy. A one-way ANOVA test was used for comparison.

This statistic compares the variance in the means of three or more groups while considering one independent variable (Mackenzie, 2018). Finally, the mean pixel values and standard deviations within the CTV<sub>HR</sub> were looked at throughout brachytherapy on DWI and ADC for patients with data for each of the five BT fractions.

## **3. Results**

### ***3.1 DW Image and ADC Map Validation***

To verify the accuracy of DW image calculation on the MR console, a comparison was conducted between the pixel values of the measured DWI set (mDWI1000) and the calculated DWI set (cDWI1000) at  $b=1000 \text{ s/mm}^2$  (Figure 7). The  $R^2$  value, which measures the goodness of fit to a linear model, was found to be 0.9923, suggesting a very strong linear relationship between the acquired and calculated DWI set. The correlation coefficients between the MATLAB-derived and console-derived ADC maps ranged from 0.9662 and 0.9913, indicating a very high positive correlation between these two sets of ADC maps. Figure 8 shows a histogram of pixel-wise differences between these two sets of ADC maps, showing a large peak at a pixel difference value of zero, with a rapid decline for non-zero differences. This indicates that the majority of corresponding pixels across the two image sets exhibit identical values. A visual comparison between the MATLAB-derived and console-derived ADC maps is provided in Figure 9. These tests validate the utilization of console-derived DW images and ADC maps for the subsequent phases of this project.

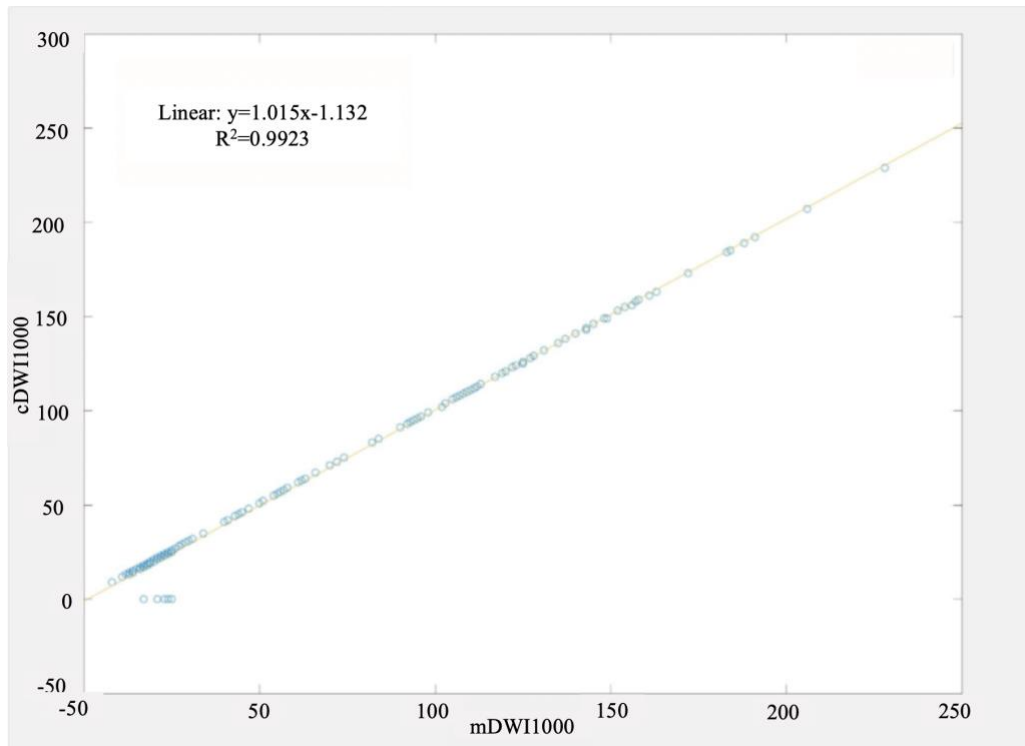


**Figure 7: Pixel values of MATLAB-derived DW image (cDWI1000) plotted against DW image from console (mDWI1000), both at  $b=1000\text{s/mm}^2$ .**

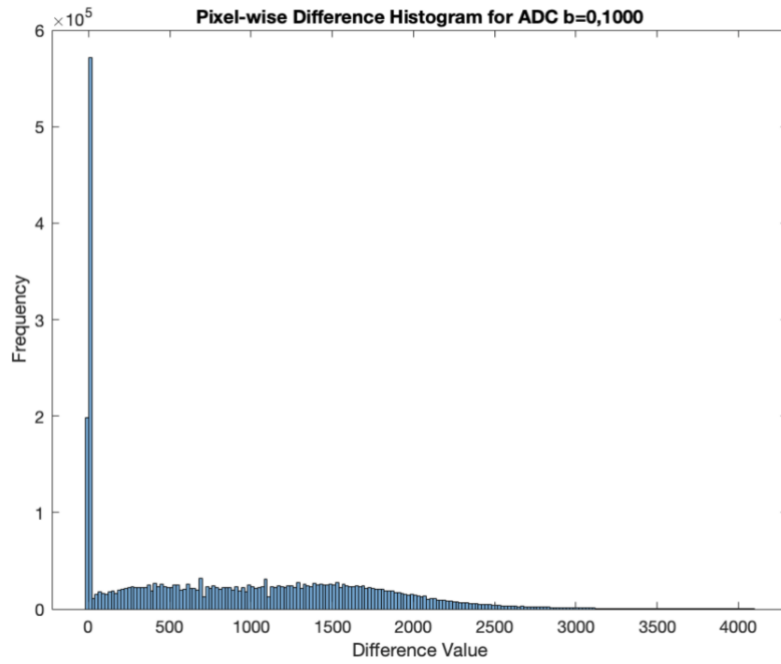


Figure 8: Pixel-wise difference histogram for MATLAB-derived and console-derived ADC maps at  $b=0,1000s/mm^2$ .

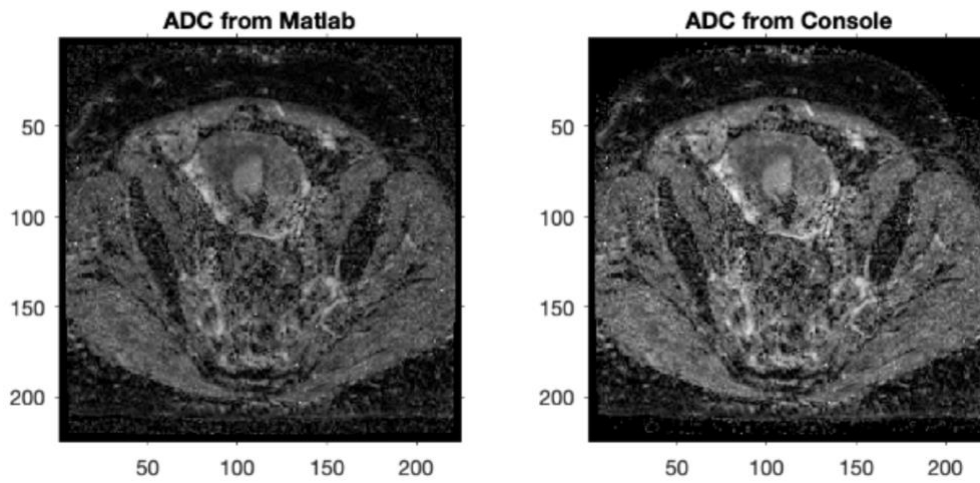


Figure 9: Visual comparison of the MATLAB-derived and console-derived ADC maps at  $b=0, 1000s/mm^2$ .

## ***3.2 Optimization of b-Value***

### **3.2.1 Quantitative Analysis**

Figure 10 depicts representative ROIs for the tumor, endometrium, endocervical canal, myometrium, and gluteal subcutaneous fat. The signal decay from  $b=1000$  to  $b=2000$   $s/mm^2$  was on average 70% for tumor and 53% for gluteal subcutaneous fat. Figure 11 illustrates the average of the CNRs across all patients for every b-value across all aforementioned anatomical structures. The average CNR for the endometrium and endocervical canal shows an increase with b-value, remains relatively stable for the myometrium, and initially decreases before rising again for the gluteal subcutaneous fat.

### **3.2.2 Qualitative Analysis**

The patients' pre-EBRT and pre-brachytherapy images at  $b=1000$ , 1300, 1600, 1800, and 2000  $s/mm^2$  for the qualitative analysis can be seen in Figure 12-16. Also shown is the axial T2 MRI. The average rankings are plotted in Figure 17, and detailed data is shown in Table 1. The best rankings for tumor conspicuity and total image quality are seen at  $b=1300$   $s/mm^2$ .

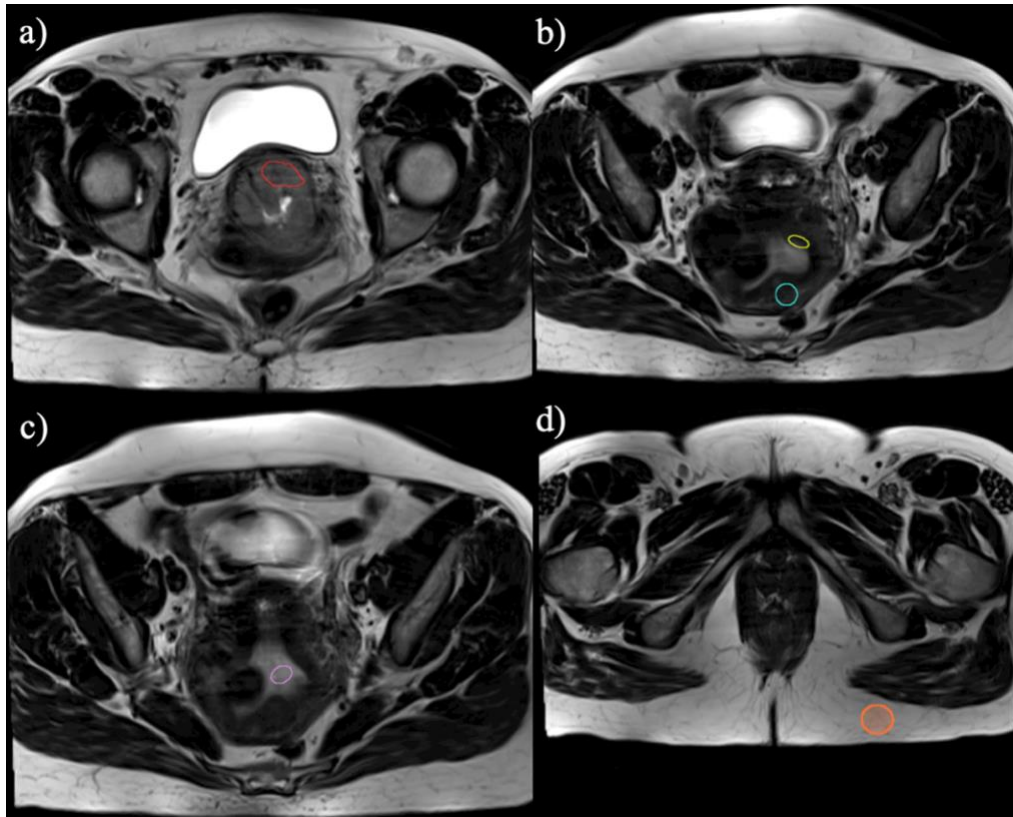


Figure 10: Example a) tumor (red), b) endometrium (yellow), myometrium (blue), c) endocervical canal (pink), and d) gluteal subcutaneous fat (orange) ROIs.

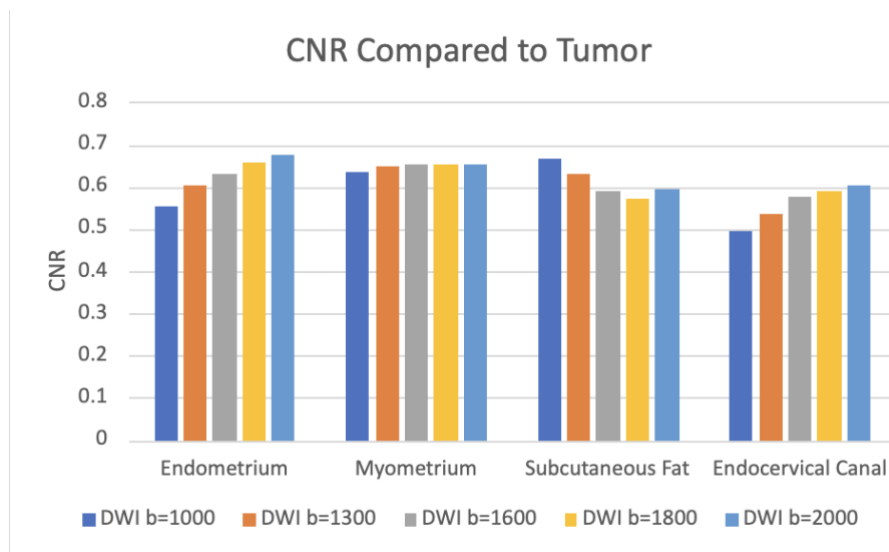


Figure 11: CNRs of each ROI compared to tumor at b=1000, 1300, 1600, 1800, and 2000 s/mm<sup>2</sup>. Plot is for pre-EBRT and pre-BT values averaged together.

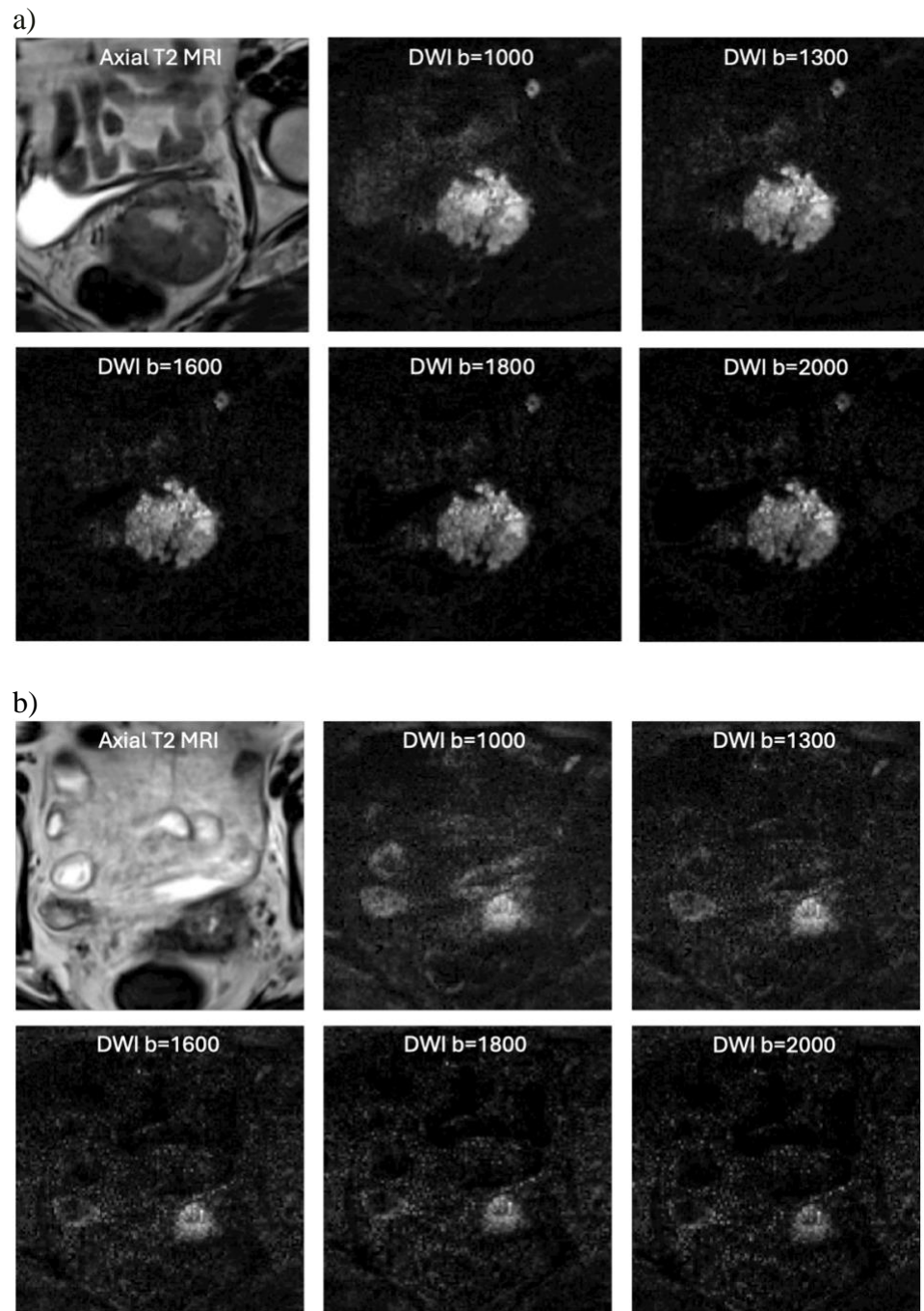


Figure 12: a) Example pre-EBRT images for Patient 1, b) and the corresponding pre-BT images. The field of view is cropped to show relevant structures.

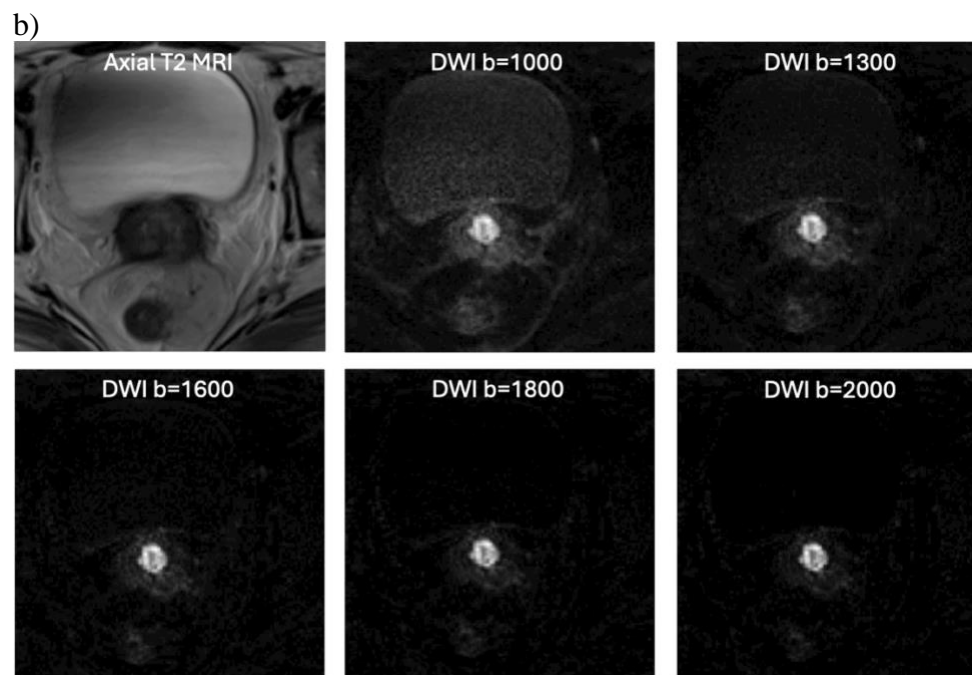
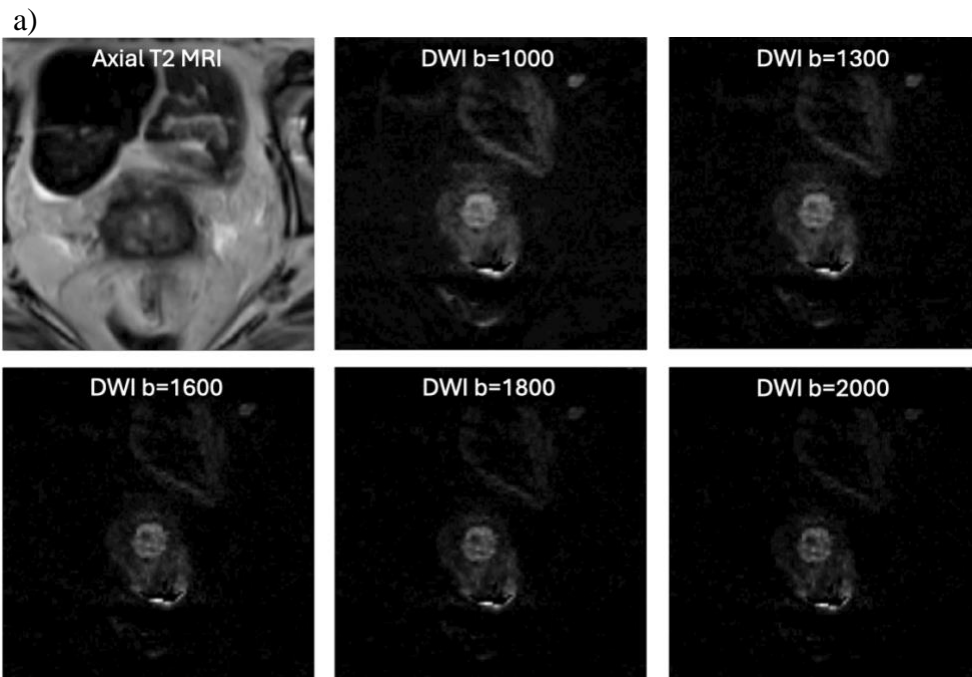
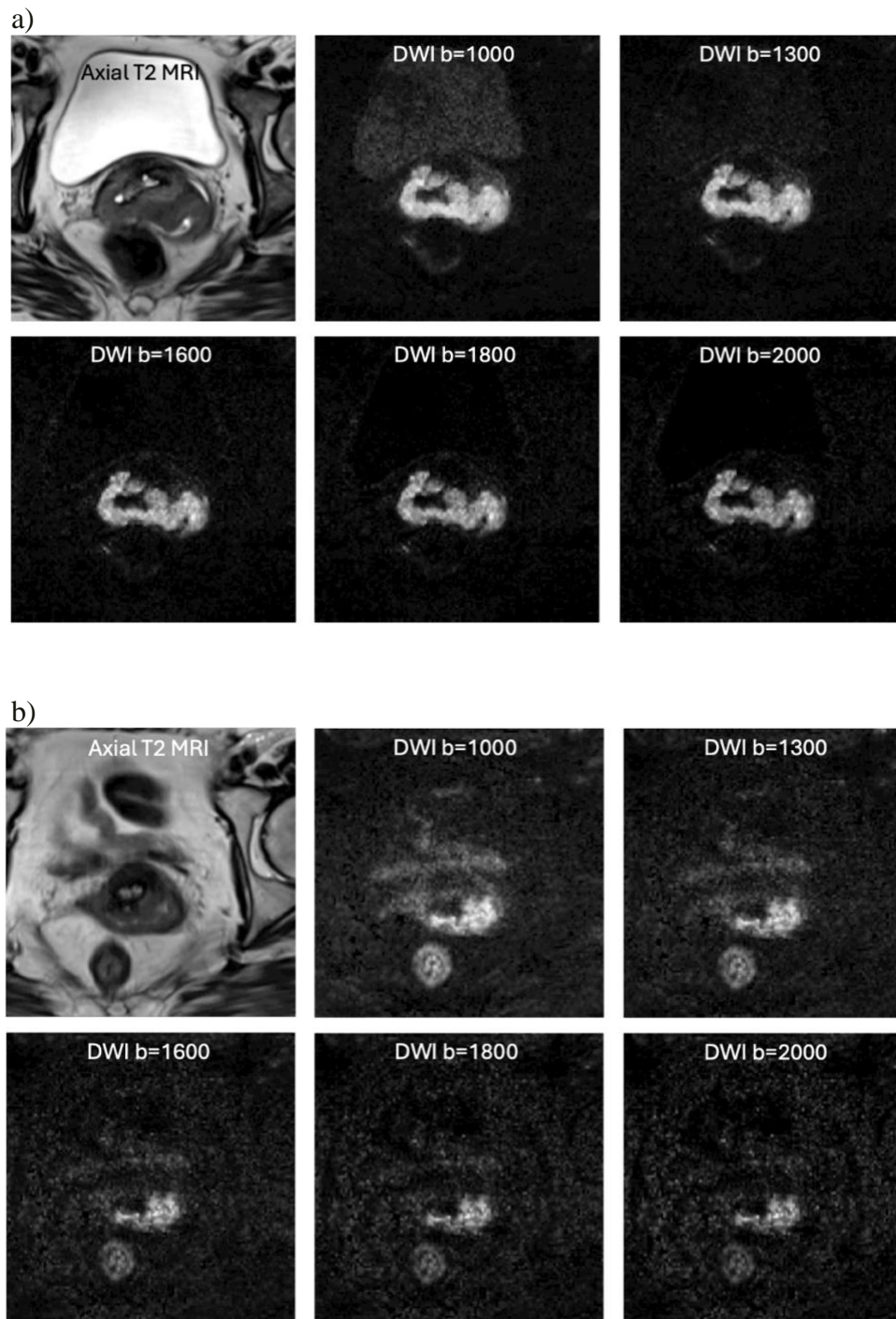


Figure 13: a) Example pre-EBRT images for Patient 2, b) and the corresponding pre-BT images. The field of view is cropped to show relevant structures.



**Figure 14: a) Example pre-EBRT images for Patient 3, b) and the corresponding pre-BT images. The field of view is cropped to show relevant structures.**

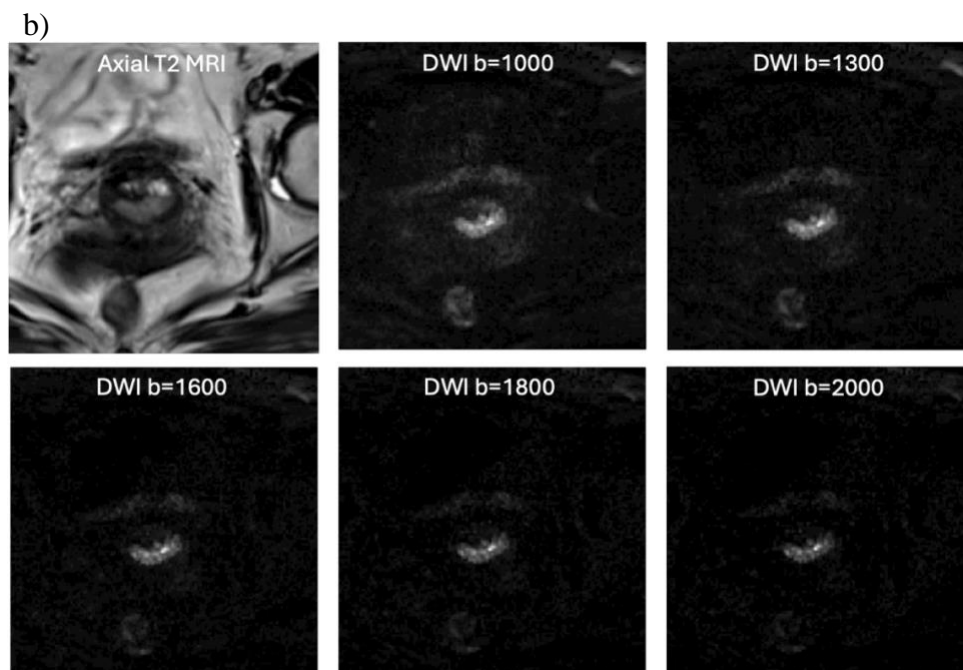
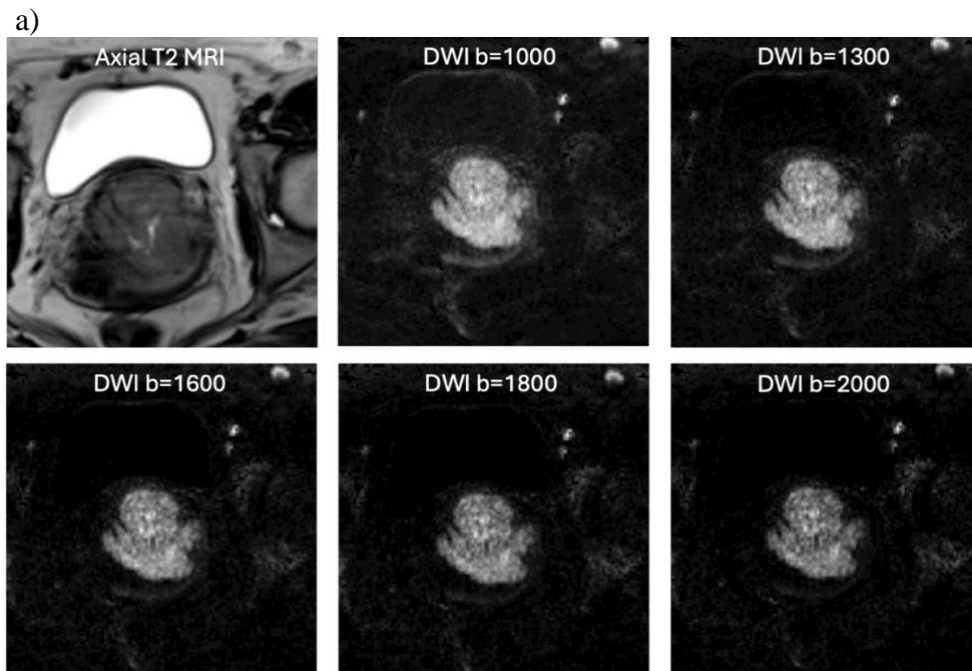
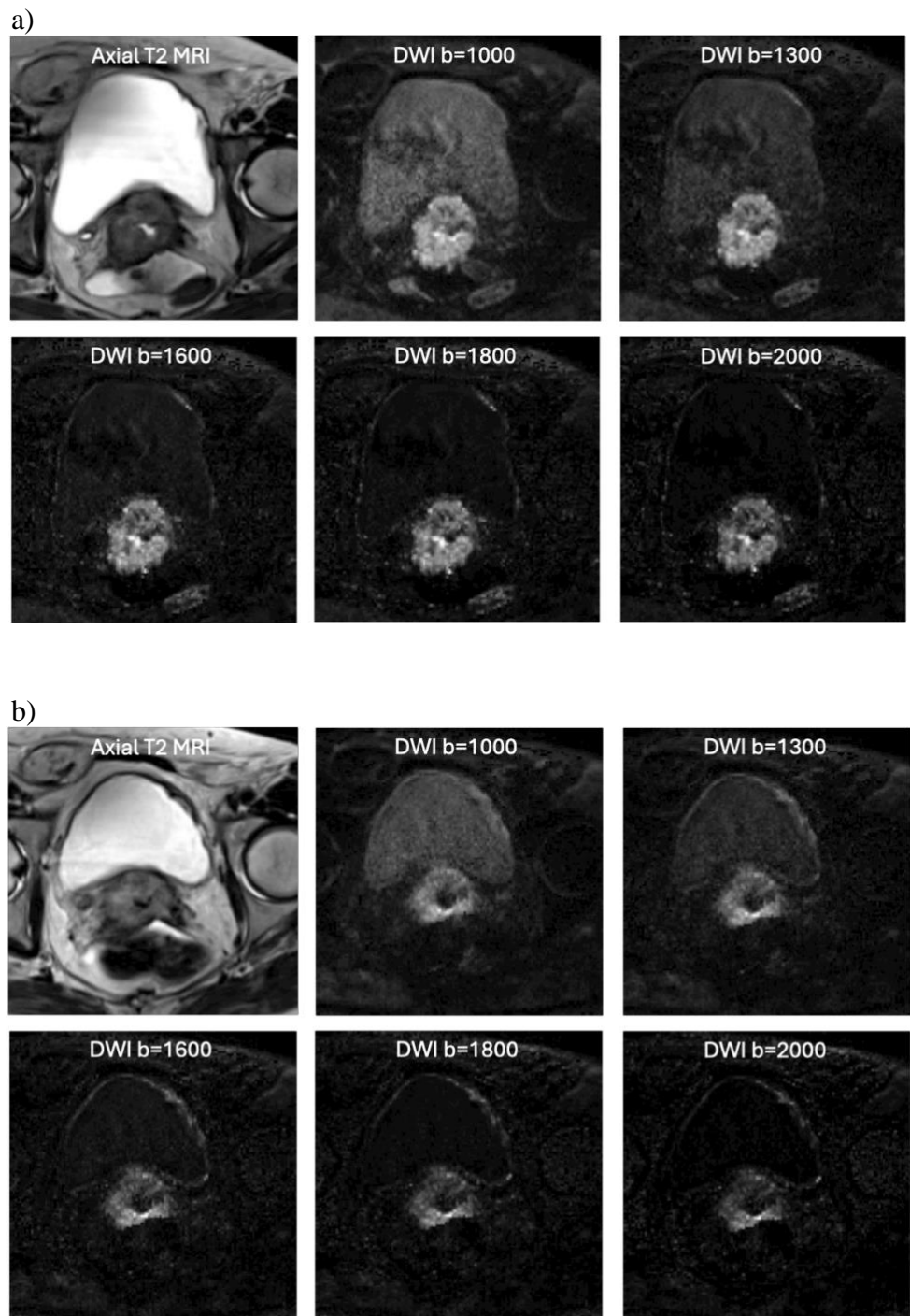


Figure 15: a) Example pre-EBRT images for Patient 3, b) and the corresponding pre-BT images. The field of view is cropped to show relevant structures.



**Figure 16: a) Example pre-EBRT images for Patient 5, b) and the corresponding pre-BT images. The field of view is cropped to show relevant structures.**

**Table 1: a) Tumor conspicuity rankings and their average values and b) total image quality rankings and their average values.**

a)

Tumor Conspicuity																					
	Physician 1										Physician 2										Average
	Patient 1		Patient 2		Patient 3		Patient 4		Patient 5		Patient 1		Patient 2		Patient 3		Patient 4		Patient 5		
	pX	pBT	pX	pBT	pX	pBT	pX	pBT	pX	pBT	pX	pBT	pX	pBT	pX	pBT	pX	pBT	pX	pBT	
b=1000	3	3	4	4	3	1	3	1	4	3	3	3	4	3	3	2	3	2	3	2	2.85
b=1300	1	1	1	2	1	2	1	2	1	2	1	1	1	1	1	1	1	1	1	1	1.2
b=1600	2	2	2	1	2	3	2	3	2	1	2	2	2	2	2	3	2	3	2	3	2.15
b=1800	4	4	3	3	4	4	4	4	3	4	4	4	3	4	4	4	4	4	4	4	3.8
b=2000	5	5	5	5	5	5	5	5	5	5	5	5	5	5	5	5	5	5	5	5	5

b)

Total Image Quality																					
	Physician 1										Physician 2										Average
	Patient 1		Patient 2		Patient 3		Patient 4		Patient 5		Patient 1		Patient 2		Patient 3		Patient 4		Patient 5		
	pX	pBT	pX	pBT	pX	pBT	pX	pBT	pX	pBT	pX	pBT	pX	pBT	pX	pBT	pX	pBT	pX	pBT	
b=1000	2	2	4	2	2	1	2	2	4	2	3	3	4	3	3	2	3	2	3	2	2.55
b=1300	1	1	1	1	1	2	1	1	1	1	1	1	1	1	1	1	1	1	1	1	1.05
b=1600	3	3	2	3	3	3	3	3	2	3	2	2	2	2	2	3	2	3	2	3	2.55
b=1800	4	4	3	4	4	4	4	4	3	4	4	4	3	4	4	4	4	4	4	4	3.85
b=2000	5	5	5	5	5	5	5	5	5	5	5	5	5	5	5	5	5	5	5	5	5

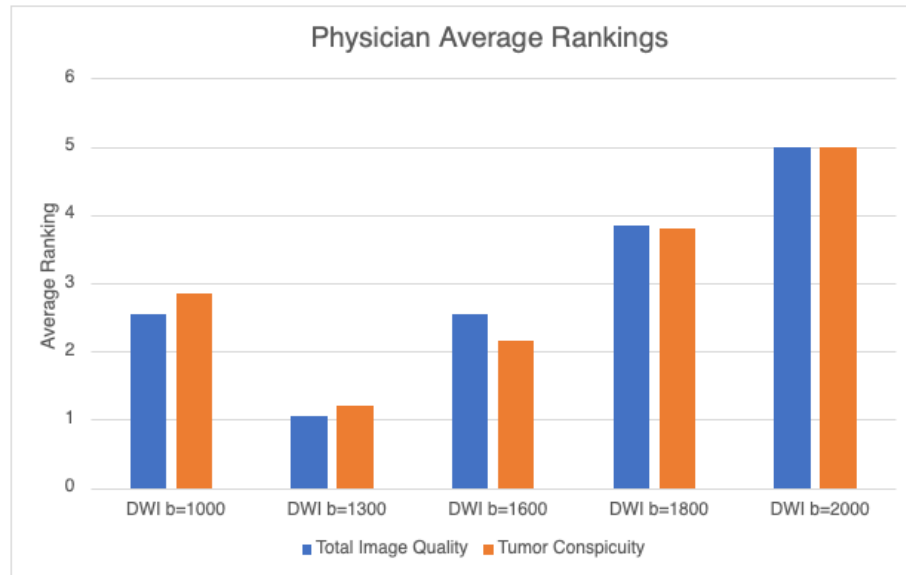


**Figure 17: Average rankings of total image quality and tumor conspicuity for each b-value.**

### ***3.3 Gross Tumor Volume (GTV) Analysis***

In the GTV analysis portion of this study, six patients were included.

Figure 18 shows an example of the pre-EBRT and pre-BT images (T2-weighted MRI, DWI and ADC) of a representative slice for one of the patients with overlaid physician-contoured GTVs. Representative images from the other five patients included in this study are shown in Appendix A.

Table 2 shows the volumes of the GTVs for each patient. In all but two cases, the pre-EBRT contoured volume is greater than the pre-BT volume. Tables 3 and 5 show the Dice coefficients and Jaccard indices of the GTVs for each patient, respectively. In each case, the pre-EBRT GTV has a higher Dice coefficient and Jaccard index than pre-BT.

Table 4 shows the Hausdorff distances for the GTVs of each patient. In four patients, each pre-EBRT Hausdorff distance is greater than its pre-BT counterpart. However, in one patient, both pre-BT Hausdorff distances are greater than pre-EBRT. Conversely, one patient's  $GTV_{DWIS}$  exhibited greater pre-EBRT Hausdorff distances, and their  $GTV_{ADCS}$  exhibited greater pre-BT Hausdorff distances.

Table 6 shows the mean pixel value of each GTV for every patient. The mean pixel value of the  $GTV_{T2WS}$  was greater for each patient in pre-EBRT compared to pre-BT, except for in Patient 5. Similarly, the mean pixel value of the  $GTV_{DWIS}$  was greater for each patient in pre-EBRT compared to pre-BT, except for in Patient 2. Also, the mean pixel value of the  $GTV_{ADCS}$  was greater for each patient in pre-BT compared to pre-EBRT, except for in Patient 2.

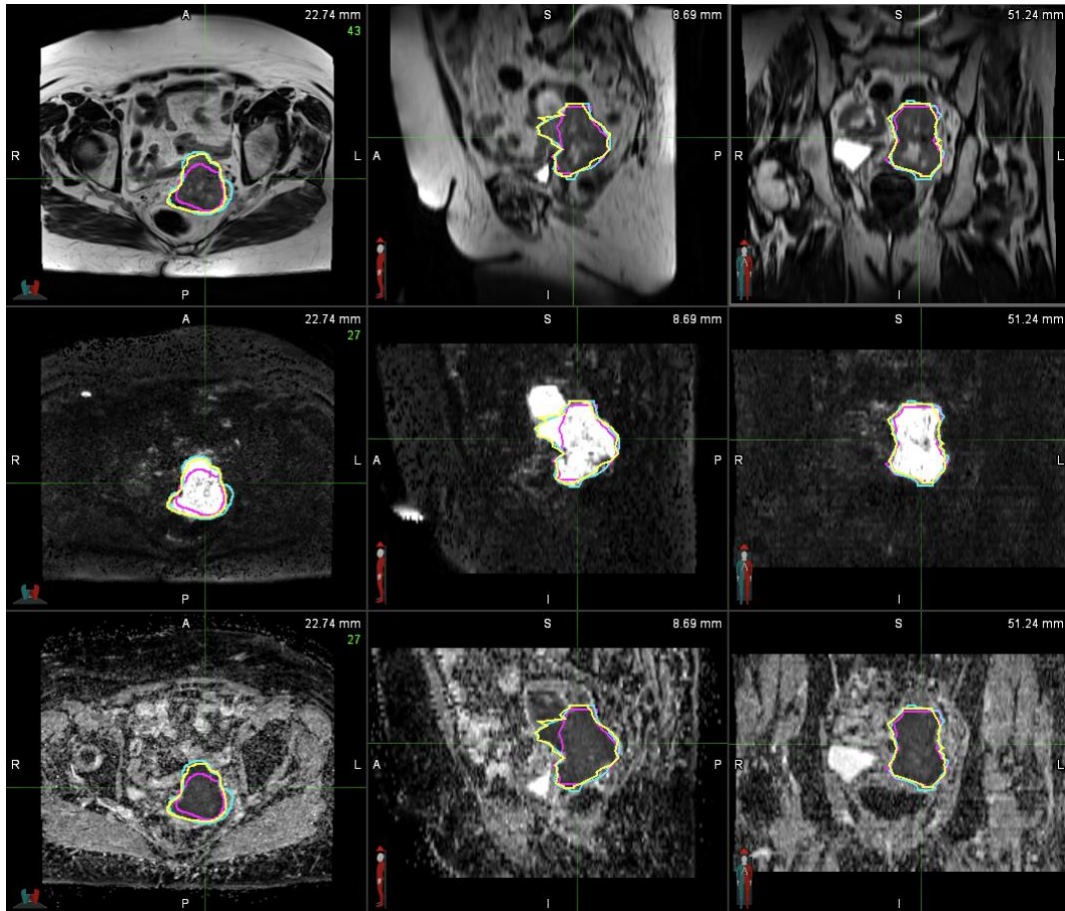
Table 7 shows the maximum pixel values for the GTVs for each patient. The maximum pixel value for the  $GTV_{T2WS}$  was greater pre-EBRT compared to pre-BT, except for in Patient 1. Similarly, the maximum pixel value for the  $GTV_{DWIS}$  was greater pre-EBRT compared to pre-BT, except for in Patient 2. The maximum pixel values of the  $GTV_{ADCS}$  do not show as much uniformity, with pre-EBRT showing higher values in Patients 2, 3, 4, and 6, while pre-BT shows higher values in Patients 1 and 5.

Table 8 shows the average statistics for all patients. The average volumes, Dice coefficients, Jaccard indices, and maximum pixel values are greater in the pre-EBRT GTVs compared to pre-BT. The average  $GTV_{DWI}$  Hausdorff distance is greater pre-

EBRT, and that of  $GTV_{ADC}$  is greater pre-BT. The average of the mean pixel values is greater pre-EBRT for both  $GTV_{T2W}$  and  $GTV_{DWI}$  and greater pre-BT for  $GTV_{ADC}$ .

Looking between  $GTV_{T2W}$ ,  $GTV_{DWI}$ , and  $GTV_{ADC}$  volumes, the  $GTV_{DWI}$  resulted in the largest volume in six out of twelve cases. Meanwhile, the  $GTV_{ADC}$  resulted in the largest volume in one out of twelve cases. Similarly, the  $GTV_{DWI}$  and  $GTV_{ADC}$  resulted in the smallest volume in two out of twelve and seven out of twelve cases, respectively. The Dice coefficients, Jaccard indices, and Hausdorff distances do not show any trends when looking between  $GTV_{DWI}$  and  $GTV_{ADC}$ .

a)



b)

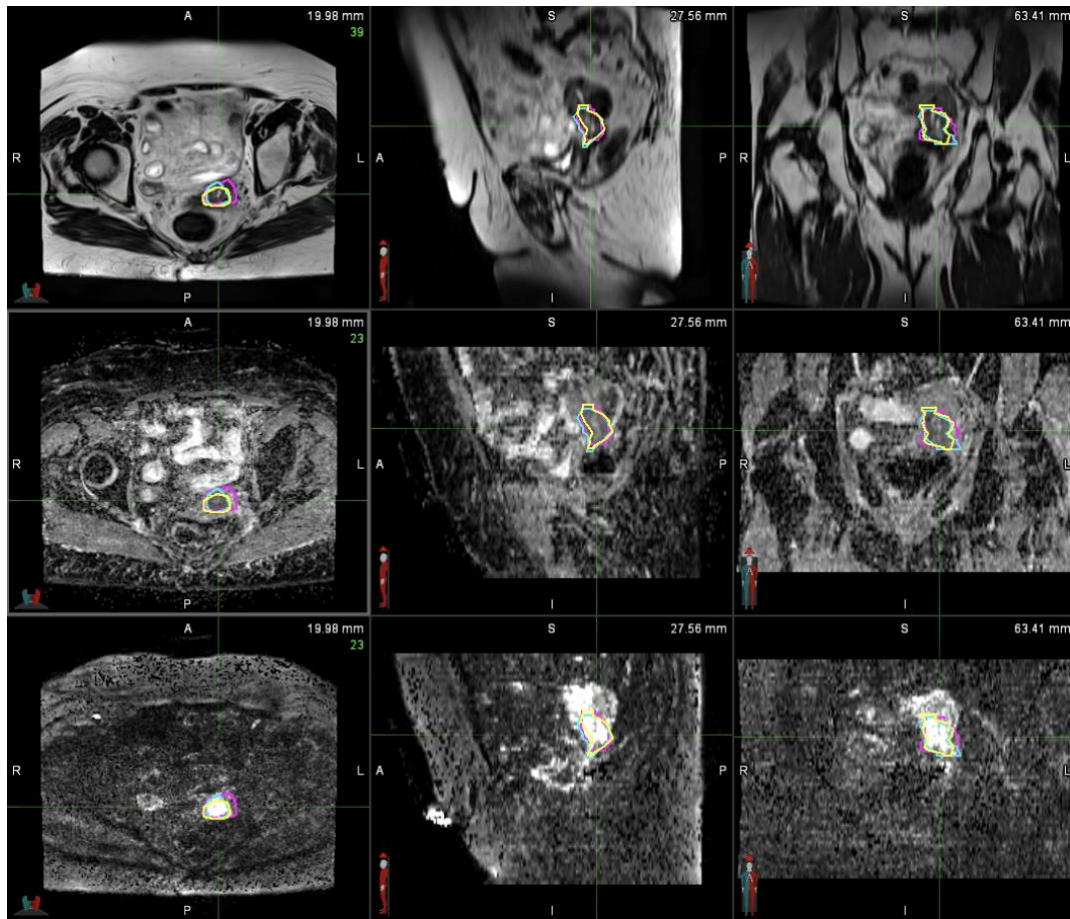


**Figure 18: Example slice from Patient 1's a) pre-EBRT scan and b) pre-brachytherapy scan with the overlaid GTVs. The image rows from top to bottom for the pre-EBRT scan are T2 MRI, DWI, and ADC. The image rows from top to bottom for the pre-brachytherapy scan are T2 MRI, ADC, and DWI. The GTVs contoured with the axial T2 MRI, with the axial T2 MRI/DWI fusion, and with the axial T2 MRI/ADC fusion are magenta, cyan, and yellow, respectively.**

**Table 2: Volume of GTV contoured on axial T2 MRI, with the help of DWI, and with the help of ADC for each patient.**

Volume (mL) of GTVs for Each Patient (Pre:Pre-EBRT, Post:Pre-Brachytherapy)						
Patient #	1	2	3	4	5	6
GTV from ax-T2 MRI	Pre: 84.02 Post: 15.18	18.27 18.64	51.1 7.44	82.33 9.29	32.21 16.14	5.52 0.39
GTV from DWI fusion	Pre: 114.15 Post: 12.64	31.31 5.95	53.45 9.34	67.35 9.65	21.53 22.72	3.91 0.67
GTV from ADC fusion	Pre: 103.88 Post: 11.24	24.43 3.17	46.15 5.79	67.91 8.49	29.99 24.05	2.64 0.25

**Table 3: Dice coefficient of GTV contoured on axial T2 MRI, with the help of DWI, and with the help of ADC for each patient.**

Dice Coefficient of GTVs for Each Patient (Pre:Pre-EBRT, Post:Pre-Brachytherapy)						
Patient #	1	2	3	4	5	6
GTV from DWI fusion	Pre: 0.81 Post: 0.75	0.71 0.47	0.8 0.73	0.84 0.76	0.76 0.75	0.56 0.49
GTV from ADC fusion	Pre: 0.82 Post: 0.74	0.8 0.29	0.8 0.69	0.81 0.8	0.8 0.73	0.58 0.15

**Table 4: Hausdorff distance of GTV contoured on axial T2 MRI, with the help of DWI, and with the help of ADC for each patient.**

Hausdorff Distance of GTVs for Each Patient						
Patient #	1	2	3	4	5	6
GTV from DWI fusion	Pre: 2.65 Post: 1.53	2.48 4.11	1.85 1.46	2.03 1.31	2.18 1.92	3.4 1.18
GTV from ADC fusion	Pre: 2.57 Post: 1.63	1.55 5.96	1.83 1.56	2.47 1.22	1.88 2.26	3.23 2.73

**Table 5: Jaccard index of GTV contoured on axial T2 MRI, with the help of DWI, and with the help of ADC for each patient.**

Jaccard Index of GTVs for Each Patient (Pre:Pre-EBRT, Post:Pre-Brachytherapy)						
Patient #	1	2	3	4	5	6
GTV from DWI fusion	Pre: 0.68 Post: 0.6	0.55 0.31	0.67 0.58	0.72 0.61	0.61 0.6	0.39 0.33
GTV from ADC fusion	Pre: 0.69 Post: 0.59	0.66 0.17	0.66 0.53	0.68 0.67	0.66 0.58	0.41 0.08

**Table 6: Mean pixel value of GTV contoured on axial T2 MRI, with the help of DWI, and with the help of ADC for each patient.**

Mean Pixel Value of GTVs for Each Patient (Pre:Pre-EBRT, Post:Pre-Brachytherapy)						
Patient #	1	2	3	4	5	6
GTV from ax-T2 MRI	Pre: 200.69 Post: 177.36	153.62 132.09	201.43 154.9	223.41 193.02	211.66 240.79	117.17 105.09
GTV from DWI fusion	Pre: 118.94 Post: 49.68	71.3 109.64	109.33 60.08	107.33 58.12	73.68 48.01	92.33 32.94
GTV from ADC fusion	Pre: 928.12 Post: 1505.35	1055.53 765.69	1010.86 1191.6	1102.13 1270.53	1164.17 1545.89	720.97 1303.26

**Table 7: Maximum pixel value of GTV contoured on axial T2 MRI, with the help of DWI, and with the help of ADC for each patient.**

Maximum Pixel Value of GTVs for Each Patient (Pre:Pre-EBRT, Post:Pre-Brachytherapy)						
Patient #	1	2	3	4	5	6
GTV from ax-T2 MRI	Pre: 548 Post: 716	406 315	1431 368	899 671	968 457	310 200
GTV from DWI fusion	Pre: 347 Post: 119	235 295	326 144	400 218	163 144	225 80
GTV from ADC fusion	Pre: 4009 Post: 4095	2491 1970	4095 2741	4095 3168	3390 3505	2759 2226

**Table 8: Average statistics of all patients for GTV contoured with axial T2 MRI, with the help of DWI, and with the help of ADC.**

Average Statistics for All Patients (Pre:Pre-EBRT, Post:Pre-Brachytherapy)						
	Volume (mL)	Dice Coefficient	Hausdorff Distance	Jaccard Index	Mean Pixel Value	Maximum Pixel Value
GTV from ax-T2 MRI	Pre: 53.59 Post: 13.34	N/A	N/A	N/A	198.16 179.63	626.2 505.4
GTV from DWI fusion	Pre: 57.56 Post: 12.06	0.78 0.69	2.24 2.07	0.65 0.54	96.12 65.11	274 184
GTV from ADC fusion	Pre: 54.47 Post: 10.55	0.81 0.65	2.06 2.53	0.67 0.51	1052.16 1255.81	3348.8 3095.4

### ***3.4 Applicator Artifact Quantification***

For one representative patient, the  $CTV_{HR}$ ,  $CTV_{HR}$ -Tandem, and  $CTV_{HR}$ -Tandem expansion can be seen overlaid on the DW images at  $b=1000, 1100, 1300, 1500, 1800,$  and  $2000 \text{ s/mm}^2$  in Figure 19. Table 9 presents the data from the preliminary quantitative analysis. The percent differences between the mean pixel values within the  $CTV_{HR}$ -Tandem and  $CTV_{HR}$ -Tandem expansion for the  $b=1000, 1100, 1300, 1500, 1800,$  and  $2000 \text{ s/mm}^2$  DW image slices are as follows: 1.92%, 1.66%, 1.24%, 0.81%, 0.23%, and 0.15%, respectively.

Figure 20 shows an example axial T2 MR image, DW image at  $b=1000 \text{ s/mm}^2$ , and ADC map at  $b=0, 1000 \text{ s/mm}^2$  from the ice water phantom experiment. The tandem is contoured in each image and no significant artifacts can be seen outside of the tandem in the axial T2 MRI, DWI, and ADC maps.

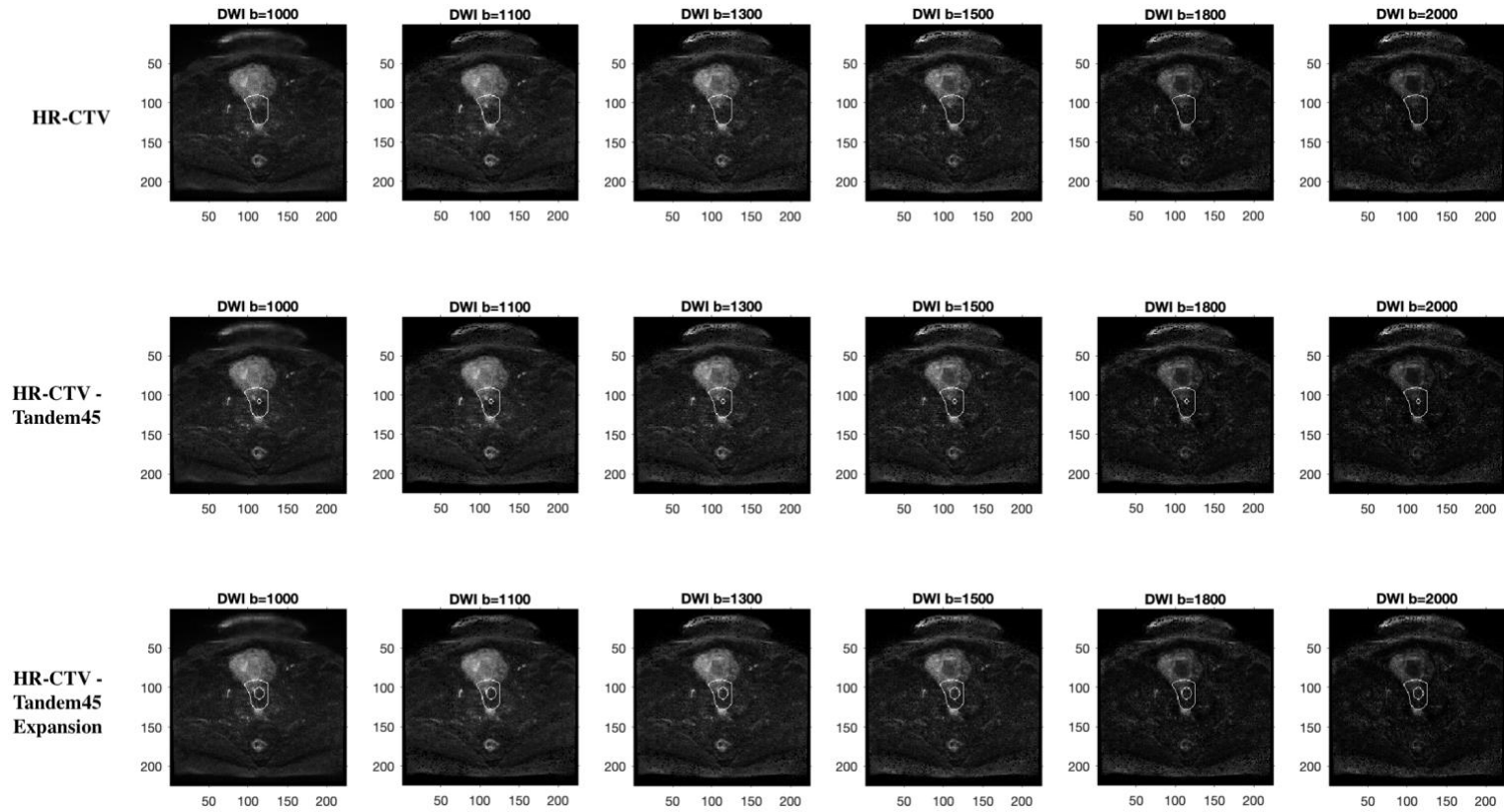
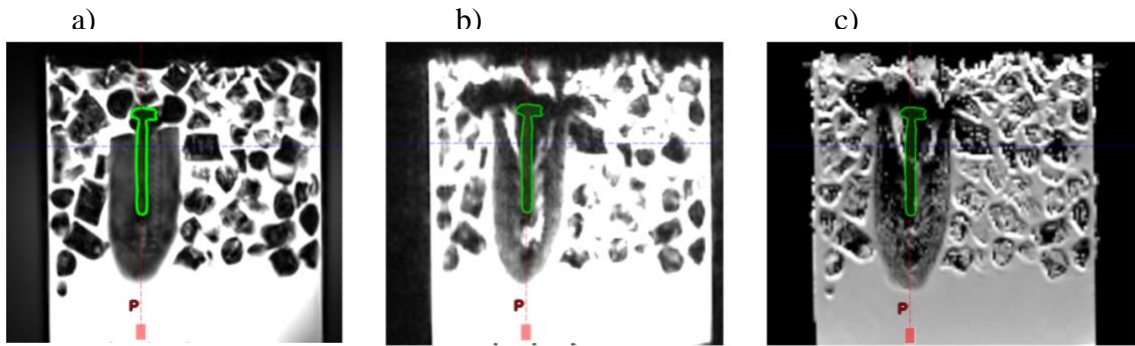


Figure 19: The  $CTV_{HR}$ ,  $CTV_{HR-Tandem}$ ,  $CTV_{HR-Tandem}$  expansion overlaid on a DW image slice at various b-value

Mean Pixel Values within CTV <sub>HR</sub>						
	b=1000	b=1100	b=1300	b=1500	b=1800	b=2000
CTV <sub>HR</sub>	30.31	25.63	18.33	13.35	8.60	6.54
CTV <sub>HR</sub> -Tandem	30.66	25.89	18.52	13.51	8.72	6.65
CTV <sub>HR</sub> -Tandem Expansion	31.25	26.32	18.75	13.62	8.74	6.64

**Table 9: Mean pixel values within the CTV<sub>HR</sub>, CTV<sub>HR</sub>-Tandem, and CTV<sub>HR</sub>-Tandem expansion on each b-value DW image.**



**Figure 20: Example slice from the ice water experiment of the a) axial T2 MRI, b) DWI at b=1000 s/mm<sup>2</sup>, and c) ADC map at b=0,1000 s/mm<sup>2</sup>. The tandem is contoured in green.**

### ***3.5 Longitudinal Analysis of CTV<sub>HR</sub>***

Fourteen patients were included in this portion of the study. An example of an CTV<sub>HR</sub> and CTV<sub>HR</sub> minus the tandem contours can be seen in Figure 21. Figures 22 and 23 show box and whisker plots of the mean pixel values within each CTV<sub>HR</sub>-tandem on the DW and ADC image sets, respectively. Overall, there is no apparent trend for the average of the mean pixel values when examining the ADC maps, but the average of

mean pixel values generally decreases throughout the brachytherapy fractions when observing the DW images. The average DWI mean pixel value decreases from 30.21 to 19.93 between fractions one and five, a 34% difference. These values are unitless. The average ADC mean pixel value increases from  $1.45 \times 10^{-3} \text{ mm}^2/\text{s}$  in fraction one to  $1.49 \times 10^{-3} \text{ mm}^2/\text{s}$  in fraction five, a 2.6% difference. However, excluding outliers, a one-way ANOVA test comparing mean pixel values on DWI and ADC throughout brachytherapy revealed a p-value of 0.1723 and 0.9453, respectively.  $p \leq 0.05$  indicates a statistically significant difference between groups, so there were no significant differences between the mean pixel values within the CTV<sub>HR</sub>-Tandem on DWI and ADC.

Figures 24 and 25 show box and whisker plots of the standard deviation of the pixel values within each CTV<sub>HR</sub>-tandem on the DW image set and ADC maps, respectively. The average DWI standard deviation decreases from 24.64 to 13.17 between fractions one and five, a 46.54% difference. These values are unitless. The average ADC standard deviation increases from  $6.88 \times 10^{-4} \text{ mm}^2/\text{s}$  to  $7.34 \times 10^{-4} \text{ mm}^2/\text{s}$  between fractions one and five, a 6.34% difference. Therefore, while the standard deviation on the ADC maps generally increases, it does so to a smaller extent. A one-way ANOVA test comparing the standard deviation of pixel values within the CTV<sub>HR</sub>-Tandem on DWI and ADC throughout brachytherapy revealed a p-value of 0.1724 and 0.7906, respectively. Therefore, there were no significant differences between the pixel value standard deviations over the course of brachytherapy on DWI and ADC.

Finally, Figure 26 shows the mean pixel values and standard deviations within the  $CTV_{HR}$  on DWI and ADC throughout brachytherapy. Individual data is shown for patients who received a DW scan for all five fractions of treatment. The patient shown in blue stands out for their higher mean pixel value on DWI and lower mean pixel value on ADC. This could be indicative of a more radio-resistant tumor. On the other hand, the patient shown in purple could be indicative of a well-responding tumor, with it exhibiting lower DWI and higher ADC means throughout treatment. The patients shown in green and red show much variation in mean pixel values and standard deviations fraction to fraction, which could indicate that their  $CTV_{HR}$ s were more challenging to contour compared to the other patients.



**Figure 21: Example  $CTV_{HR}$  contour (left) and  $CTV_{HR}$ -tandem contour (right).**

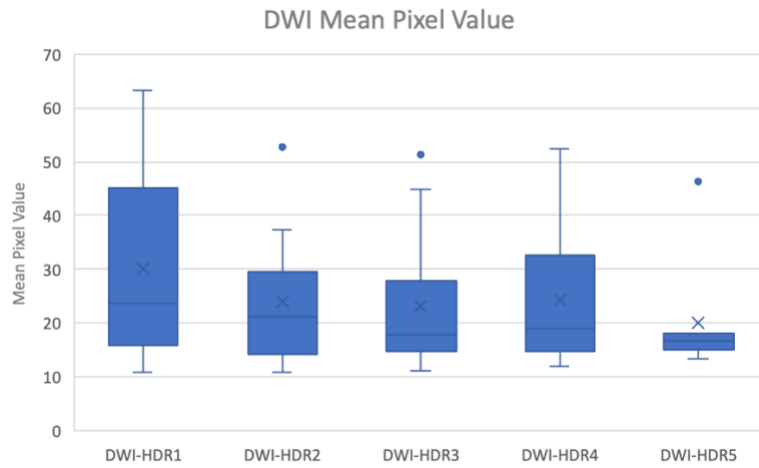


**Figure 22: Box and whisker plot of the mean pixel values within each CTV<sub>HR</sub>-tandem on the DW image set.**

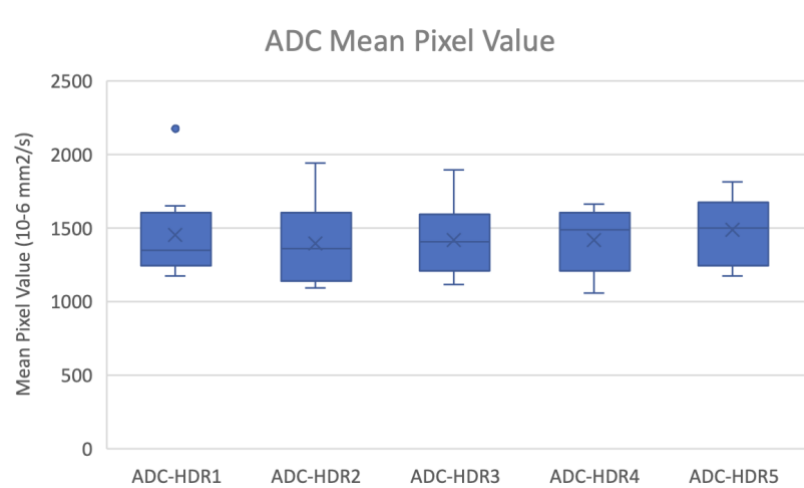


**Figure 23: Box and whisker plot of the mean pixel values within each CTV<sub>HR</sub>-tandem on the ADC maps.**

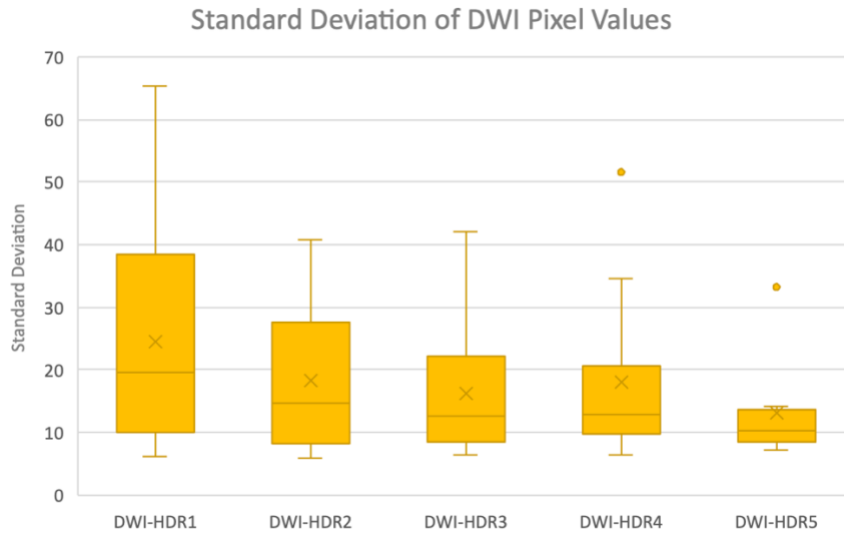


**Figure 24: Box and whisker plot of the standard deviation of the pixel values within each CTV<sub>HR</sub>-tandem on the DW image set.**

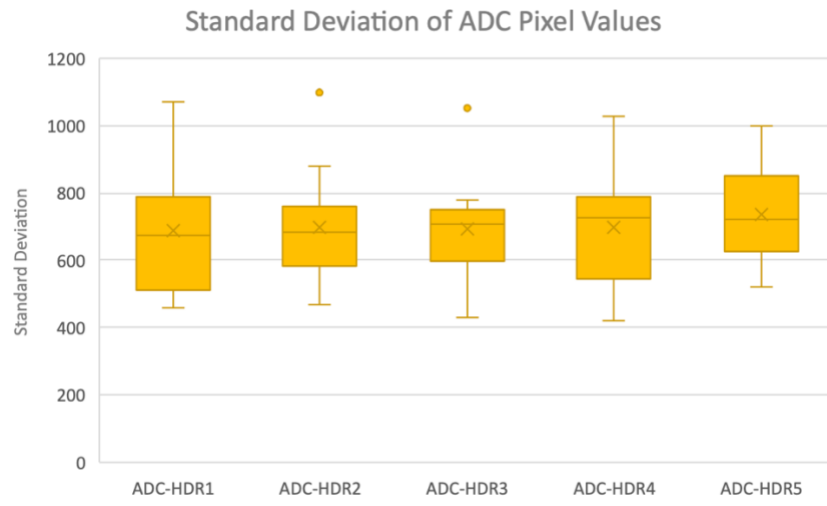


**Figure 25: Box and whisker plot of the standard deviation of the pixel values within each CTV<sub>HR</sub>-tandem on the ADC maps.**

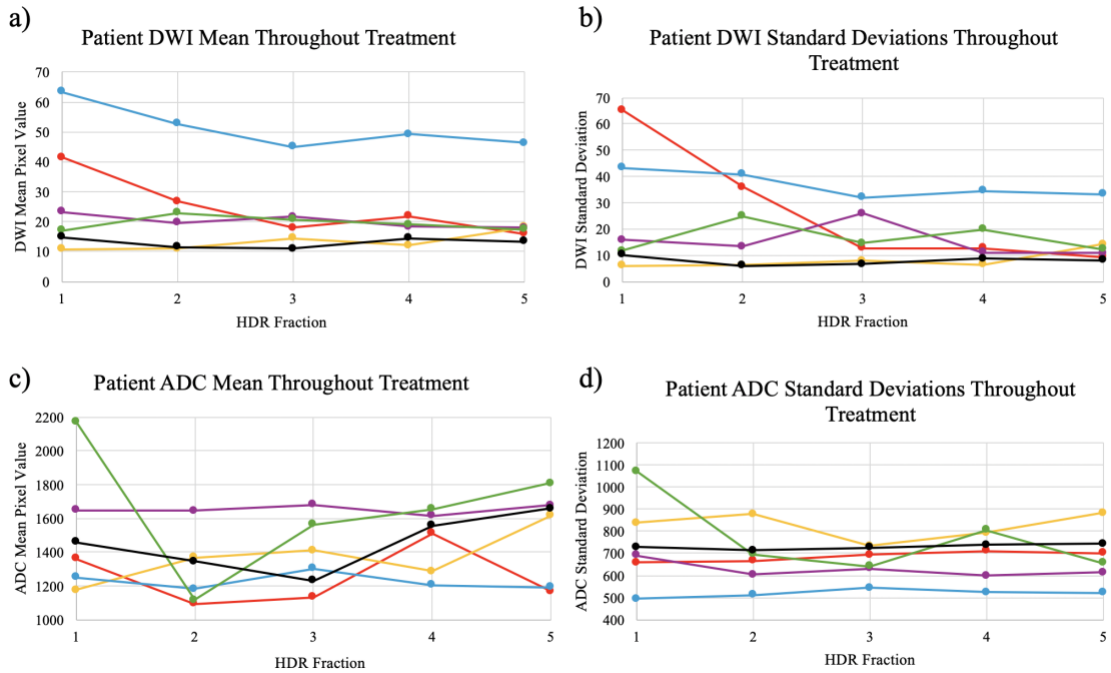


Figure 26: a) Patient mean pixel values on DWI, b) standard deviations on DWI, c) mean pixel values on ADC, d) and standard deviations on ADC throughout BT.

## 4. Discussion

### 4.1 Optimization of *b*-Value

This study sought to validate and optimize DW imaging for GYN applications and to evaluate its potential clinical applications in the management of GYN cancer patients undergoing EBRT and HDR brachytherapy. After validating the use of MR console-generated DWI and ADC maps via an in-house MATLAB code, *b*-value optimization was accomplished through a quantitative analysis of different contrast-to-

noise ratios (CNRs) and a qualitative analysis involving two physician's ranking tumor conspicuity and total image quality for different b-value sets. Next, the role of DWI/ADC maps in GTV contouring pre-EBRT and pre-BT was investigated by integrating their use into the contouring workflow and calculating similarity metrics. The final component of this study analyzed CTV<sub>HR</sub> pixel changes throughout the course of brachytherapy on axial T2 MR image sets, DW image sets, and ADC maps.

The selection of appropriate b-values, indicative of the degree of diffusion weighting applied, is guided by previous literature (Kuang et al, 2014; Moribata et al, 2015). By aligning our study's b-value selection methods with those of previous research, we aim to enhance the reliability and reproducibility of our findings.

The substantial signal loss seen from  $b=1000$  to  $2000 \text{ s/mm}^2$  compromises image quality. Thus, despite the higher CNRs observed for the endometrium, subcutaneous fat, and endocervical canal at  $b=2000 \text{ s/mm}^2$ , this b-value is not optimal for GTV delineation. Moreover, the CNRs for the endometrium and endocervical canal are lowest at  $b=1000 \text{ s/mm}^2$ , suggesting suboptimal CNR optimization for all ROIs at this b-value. Consequently,  $b=1300$ ,  $1600$ , and  $1800 \text{ s/mm}^2$  emerge as the most suitable b-values for GTV contouring. Further, the qualitative data indicates that the radiation oncologists generally perceive  $b=1300 \text{ s/mm}^2$  as offering the best tumor conspicuity and total image quality, showing their preference for contouring on these image sets. Combining the quantitative and qualitative data, the optimal b-value for GTV contouring in GYN cancer patients undergoing EBRT and HDR brachytherapy was determined to be  $b=1300 \text{ s/mm}^2$ .

This is similar to the findings of a previous study, which found that DW images at  $b=1300$  and  $b=1600$  s/mm<sup>2</sup> gave the best tumor conspicuity and overall image quality in cervical cancer patients compared to  $b=800$ ,  $1000$ , or  $2000$  s/mm<sup>2</sup> (Moribata et al, 2015). This study validates the findings of Moribata et al, while expounding on their time points and statistical methods, all while generalizing their results to GYN patients as opposed to only cervical cancer patients.

#### ***4.2 Gross Tumor Volume (GTV) Analysis***

In this study, something to note is that the b-value used to calculate the DW images and ADC maps for contouring was  $b=1300$  s/mm<sup>2</sup> and  $b=0$ ,  $1000$  s/mm<sup>2</sup>, respectively. The b-value chosen for ADC map calculation was  $b=0$ ,  $1000$  s/mm<sup>2</sup> because the ADC value theoretically does not change with b-value. Therefore, ADC maps calculated using  $b=0$ ,  $1300$  s/mm<sup>2</sup> would yield the same results as those calculated using  $b=0$ ,  $1000$  s/mm<sup>2</sup>. Additionally, six patients were included in this phase of the study.

For each patient, the Dice coefficients and Jaccard indices for the pre-EBRT scans were greater than their pre-BT counterparts. This could be because larger tumor volumes are easier for physicians to contour, and tumor volumes are generally larger prior to EBRT. Since tumors are generally denser than normal tissue, they experience less diffusion and would appear brighter on DWI, which is corroborated by five out of six  $GTV_{DWIS}$  exhibiting higher means prior to EBRT. Before EBRT, the GTV is more disease-ridden, restricts diffusion more, and results in higher signal. The same logic can be used for the ADC maps, since the mean pixel value in the  $GTV_{ADCs}$  was lower in pre-

EBRT for five out of six patients. Tumors are generally denser than normal tissue, experience less diffusion, and would appear darker on ADC. Before EBRT, the GTV is more disease-ridden, restricts diffusion more, and results in lower signal on ADC maps. This is supported by various studies that have shown malignant lesions have lower ADC values compared to benign lesions and normal tissue (Haack et al, 2010; Fujii et al, 2008; Tamai et al, 2008; Nagawana et al, 2005). Dalah et al also found a similar result for ADC means pre- and post-treatment for pancreatic cancer.

Further, the maximum pixel value for all GTV types tended to be greater in pre-EBRT compared to pre-BT, which is not as expected. Since denser tissue is darker on ADC and T2W MRI, one would expect the maximum pixel value of the GTV to be lower prior to EBRT when more disease is present and higher after EBRT when less disease is present. The opposite is expected for DWI and was observed in this study.

The  $GTV_{DWI}$  more often resulted in the largest contoured volume compared to  $GTV_{ADC}$ , and the  $GTV_{ADC}$  more often resulted in the smallest contoured volume, which could be indicative of ADC maps highlighting smaller more-disease ridden areas compared to DWI. However, the lack of statistical significance between the  $GTV_{DWI}$  and  $GTV_{ADC}$  metrics could indicate that DW imaging and their derived ADC maps are both comparable when implemented into the contouring workflow. More patients are needed to obtain a more robust statistical result, as no direct comparisons have been made between DWI and ADC in the literature to the best of our knowledge.

### ***4.3 Applicator Artifact Quantification***

In the preliminary quantitative artifact analysis, the minor difference in mean pixel values within the CTV<sub>HR</sub>-Tandem and CTV<sub>HR</sub>-Tandem expansion suggests that utilizing the CTV<sub>HR</sub>-Tandem is sufficient for the longitudinal analysis. Also, no significant artifacts were observed in the axial T2 MRI, DWI, or ADC map beyond the contour of the tandem in the ice water phantom experiment utilized for artifact quantification, further suggesting that subtracting the tandem, if present, from each CTV<sub>HR</sub> in the longitudinal flow is adequate. Hence, all patients analyzed with a tandem applicator had the tandem subtracted from the CTV<sub>HR</sub> of each HDR fraction prior to analysis. The extent of artifact present in DW images depends largely on the acquisition parameters, field strength, and the shape and orientation of the applicator, and a larger study is needed on artifact quantification in GYN for more robust results (Soliman et al).

### ***4.4 Longitudinal Analysis of CTV<sub>HR</sub>s***

The variability seen in the mean pixel values of DW images could suggest that DW images are not consistent enough for assistance with the contouring of the CTV<sub>HR</sub>. Moreover, the decreasing trend in standard deviations on the DW images could be due to an increase in tumor homogeneity throughout brachytherapy. However, this is not as expected, as irradiated tumors experience more genetic instability which results in increased heterogeneity (Huang et al, 2003).

Regarding ADC maps, the small percent increase of the mean pixel values and standard deviations from fraction one to five, indicates that ADC maps may provide a more consistent look at the CTV<sub>HR</sub> for assisting radiation oncologists in contouring compared to DWI. For example, Onodera et al found that various ADC histogram metrics of the uterus, such as mean, median, and maximum, were highly repeatable biomarkers, while ADC skewness and kurtosis were not as robust. However, the lack of statistical significance could indicate otherwise.

Looking at individual patients throughout BT, the patient shown in blue in stands out for their higher mean pixel value on DWI and lower mean pixel value on ADC. This could be indicative of a more radio-resistant tumor. On the other hand, the patient shown in purple could be indicative of a well-responding tumor, with it exhibiting lower DWI and higher ADC means throughout treatment. The patients shown in green and red show much variation in mean pixel values and standard deviations fraction to fraction, which could indicate that their CTV<sub>HRS</sub> were more challenging to contour compared to the other patients.

#### **4.4.1 Limitations**

Despite our findings, this study has several limitations. First, Equation 1 assumes a monoexponential relationship between the signal and diffusion coefficient, which may oversimplify tissue environments. However, a monoexponential model is the most commonly used model for diffusion-weighted imaging. Studies have looked at the use of different diffusion models in various sites, with the stretched exponential model

and intravoxel incoherent motion showing promise over more simplified models (Song et al, 2022; Bennett et al, 2003). Also, this study is limited by the number of patients analyzed. The small sample size was due to several reasons: 1) limitations imposed by the IRB-approval protocol, 2) challenges associated with accessing data from the scanner, which has a limited lifespan and becomes increasingly difficult to retrieve once deleted, and 3) the rarity of patients undergoing pre-EBRT scans, as the pre-EBRT DW sequence is often the first to be omitted in cases of scheduling constraints or patient non-cooperation. Future research should focus on expanding the patient sample size and exploring alternative diffusion models to address these limitations. Also, cutoff ADC values have been utilized in several studies, and this is a possible avenue for future research (Haack et al, 2010; Ho et al, 2016; Mukuda et al, 2016; Motoshima et al, 2011). Finally, this study is limited by its retrospective nature.

## 5. Conclusion

Through qualitative and quantitative analyses performed on both pre-EBRT and pre-brachytherapy image sets, considering radiation-induced tissue changes, this study found that the optimal b-value for DW image calculation for GYN patients is 1300 s/mm<sup>2</sup>. Five out of six GTVs, contoured with the help of DWI and ADC, exhibited higher and lower means, respectively, prior to EBRT, indicating the presence of denser, more disease-ridden tumors. Further, the maximum pixel values for the GTVs contoured using axial T2 MRI alone and in combination with ADC tended to be greater prior to EBRT compared to prior to brachytherapy, contrary to expected trends. Furthermore, GTVs contoured with the help of DWI frequently yielded the largest contoured volumes, while those contoured with the help of ADC tended to result in the smallest contoured volume, potentially suggesting that ADC maps highlight smaller more-disease ridden areas compared to DWI. However, this lacked statistical significance. To the best of our knowledge, the direct comparison between DWI and ADC map utilization in GTV contouring is not present in the literature and is an area of further study.

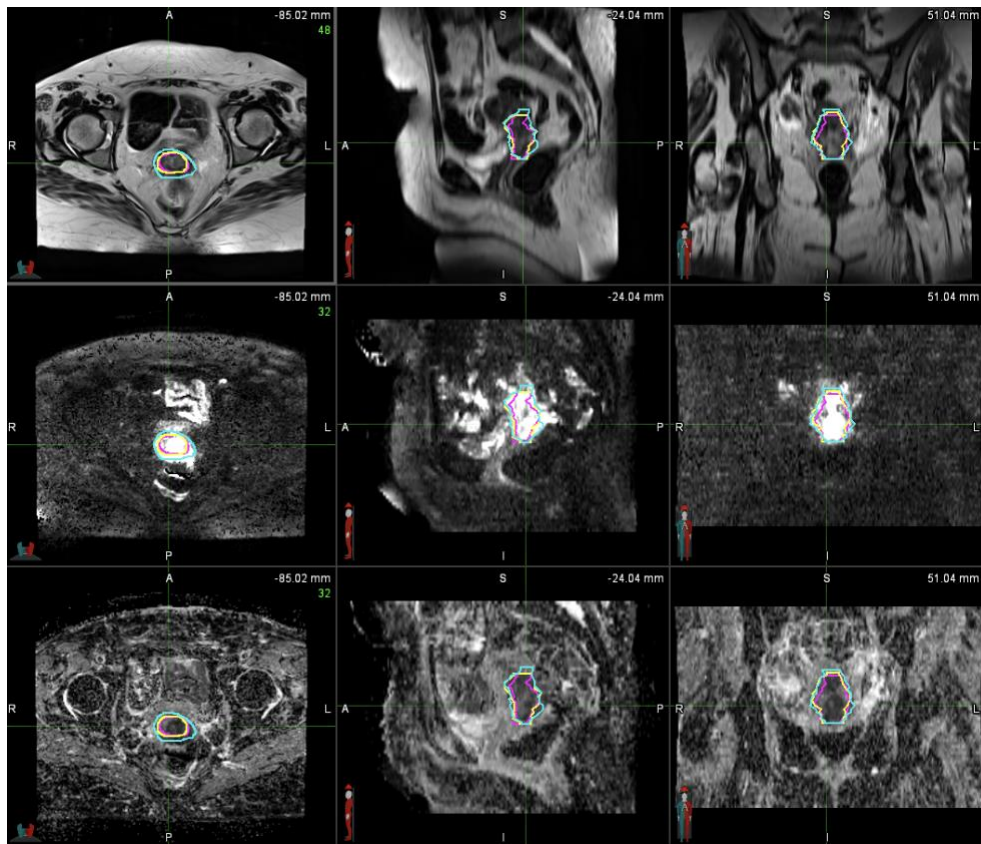
Applicator artifact quantification revealed that subtracting the tandem from the CTV<sub>HRS</sub> was adequate for use in the longitudinal analysis. More consistent mean pixel values and standard deviations within the CTV<sub>HR</sub> minus tandem volume were observed throughout brachytherapy on ADC maps compared to DW images. Moreover, the decreasing trend in standard deviation on the DW images indicated an increase in tumor homogeneity throughout brachytherapy, which could possibly be due to the tissue

response to radiation. Overall, a larger sample size is necessary to provide more insight into each modality's utility during the contouring workflow and the changes in pixel values on these modalities throughout brachytherapy.

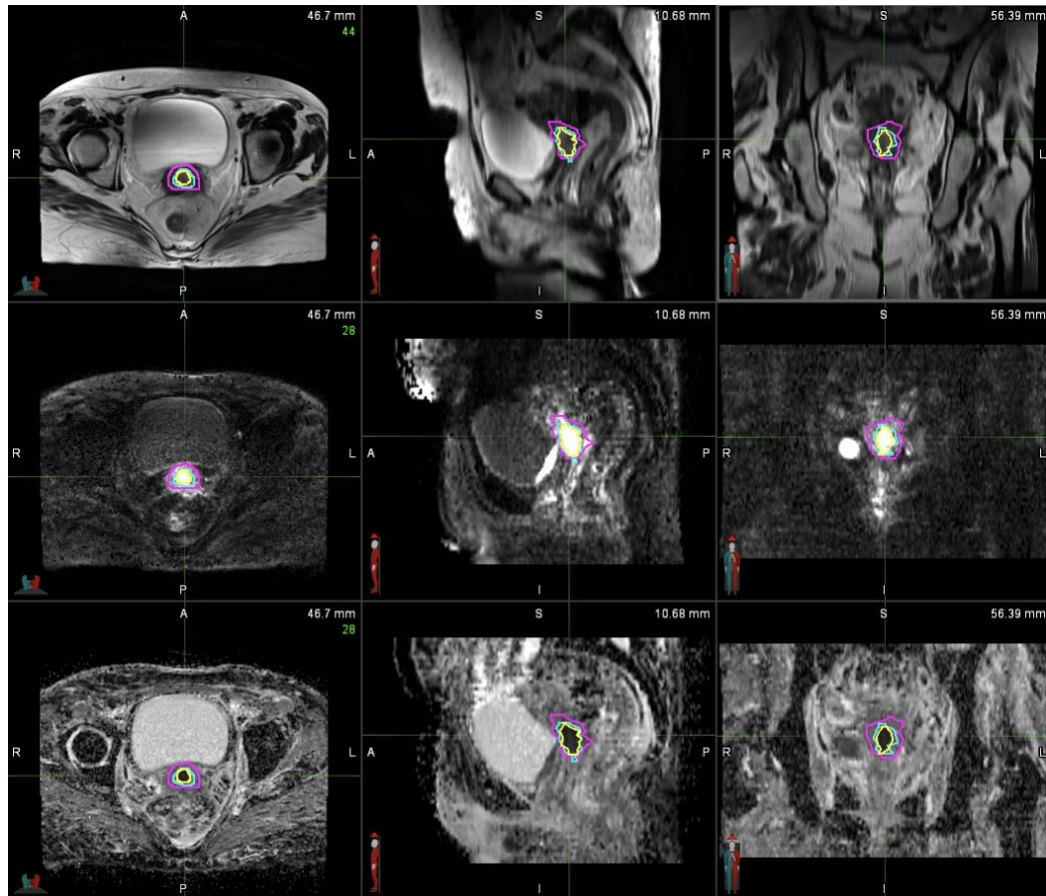
## Appendix A

Figures A1-A5 depict representative image slices from Patients 2-6 with the  $GTV_{T2W}$ ,  $GTV_{DWI}$ , and  $GTV_{ADC}$  overlays. The representative slices are shown on the axial T2 MRI, DWI, and ADC map.

a)

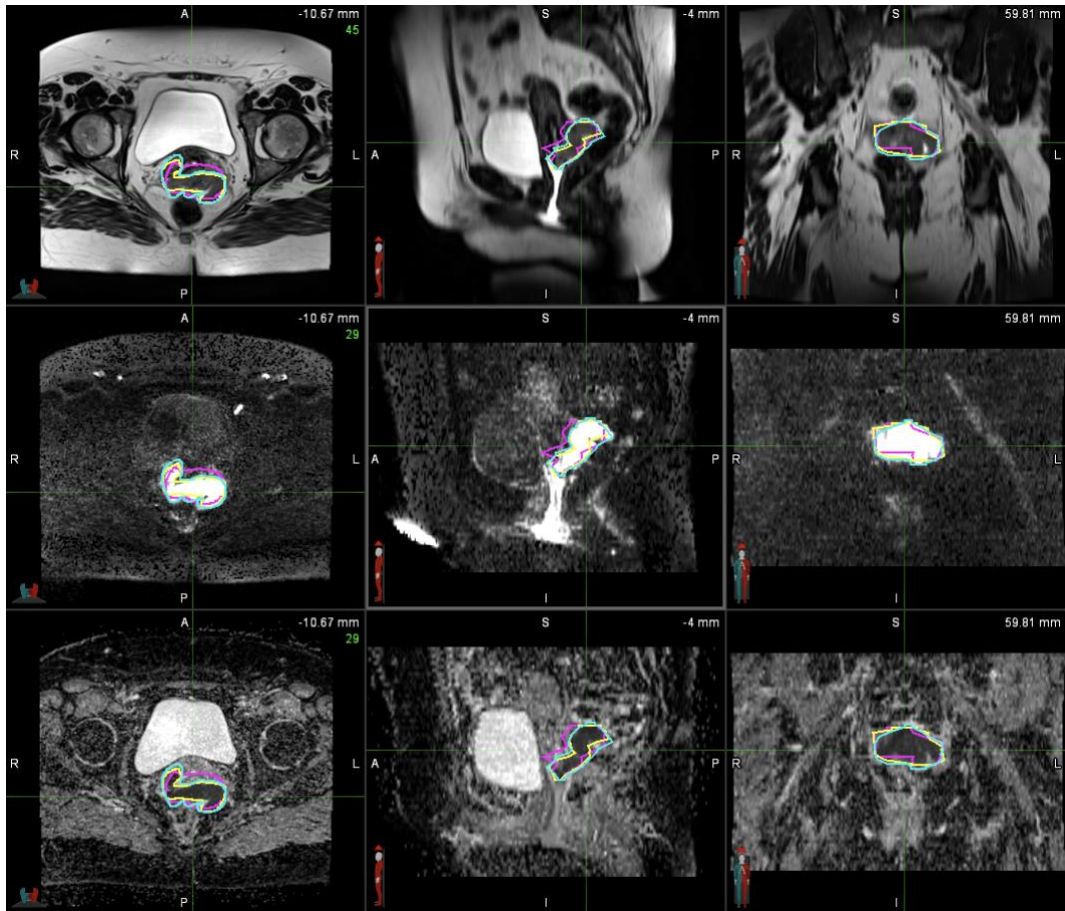


b)



**Figure A1: Example slice from Patient 2's a) pre-EBRT scan and b) pre-brachytherapy scan with the overlaid GTVs. The image rows from top to bottom for both scans are T2 MRI, DWI, and ADC. The GTVs contoured with the axial T2 MRI, with the axial T2 MRI/DWI fusion, and with the axial T2 MRI/ADC fusion are magenta, cyan, and yellow, respectively.**

a)



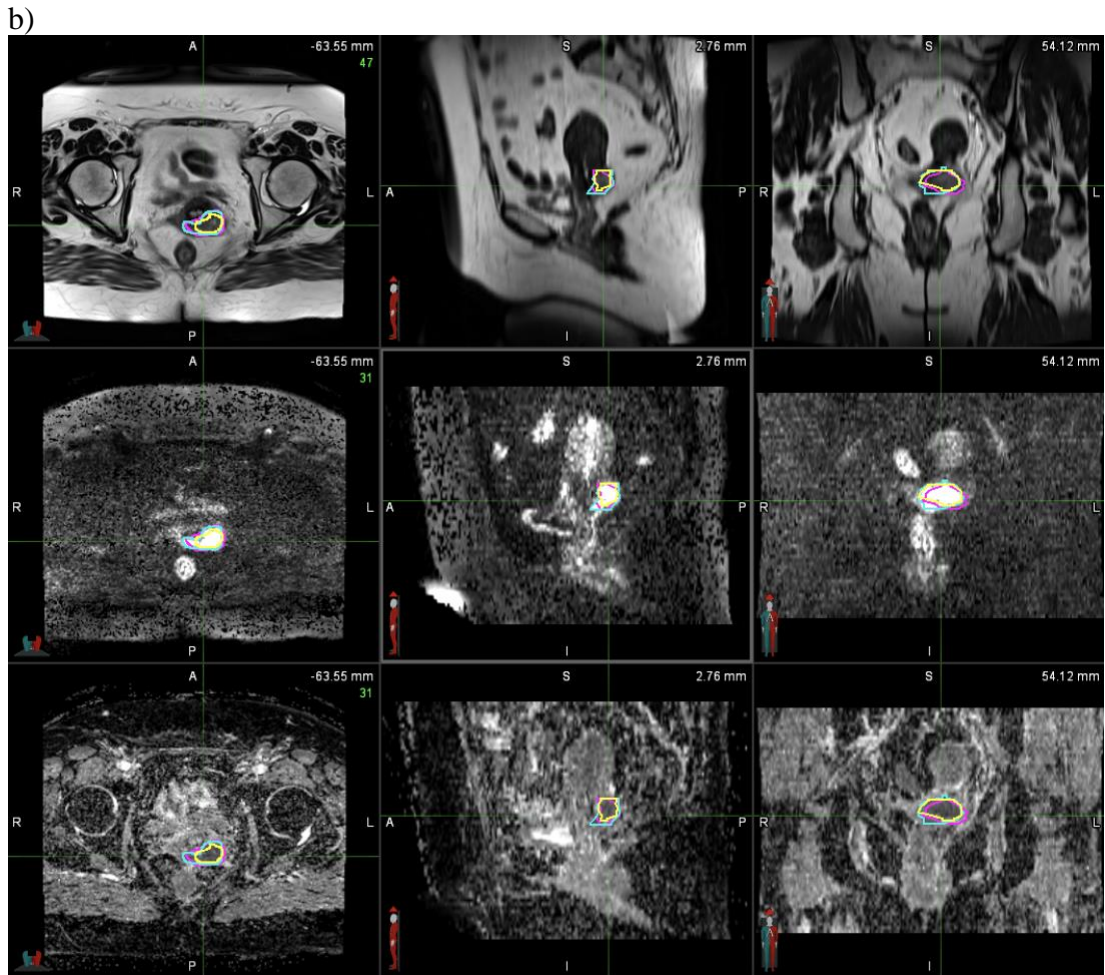
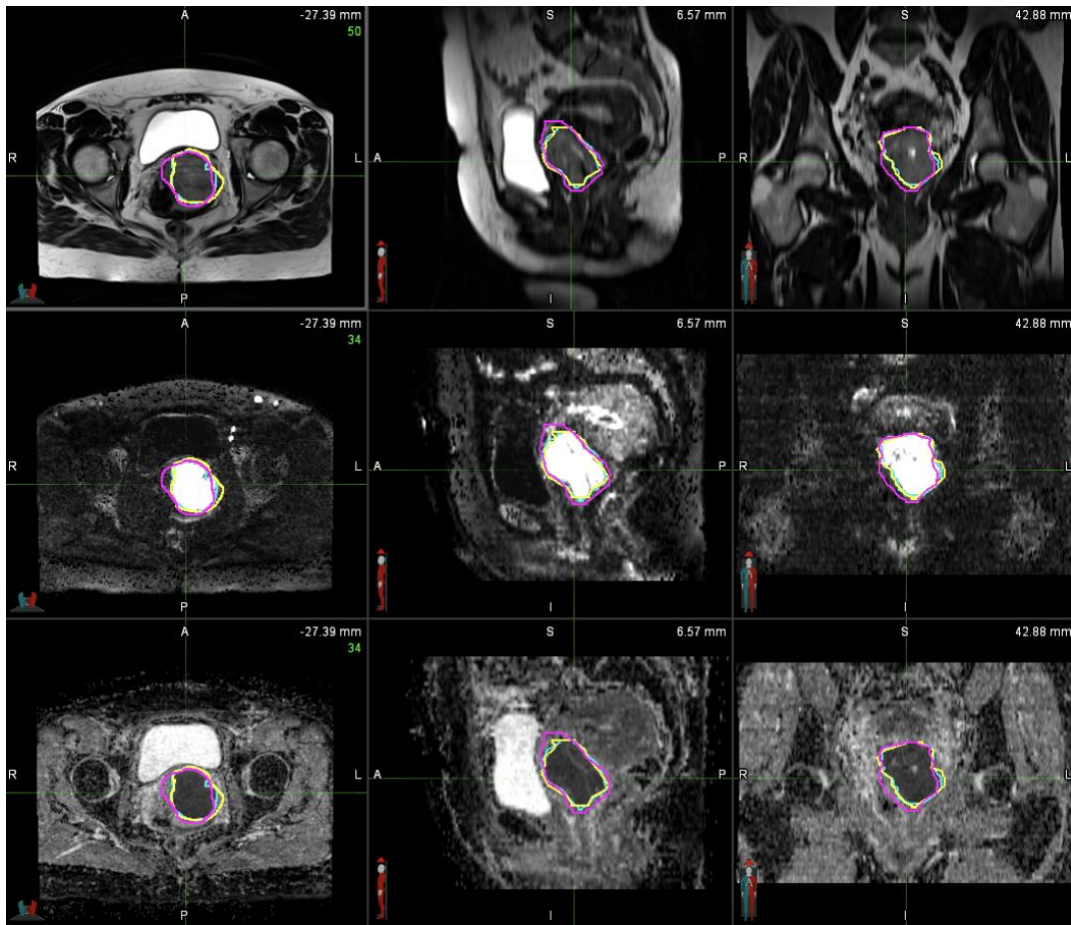


**Figure A2: Example slice from Patient 3's a) pre-EBRT scan and b) pre-brachytherapy scan with the overlaid GTVs. The image rows from top to bottom for both scans are T2 MRI, DWI, and ADC. The GTVs contoured with the axial T2 MRI, with the axial T2 MRI/DWI fusion, and with the axial T2 MRI/ADC fusion are magenta, cyan, and yellow, respectively.**

a)



b)

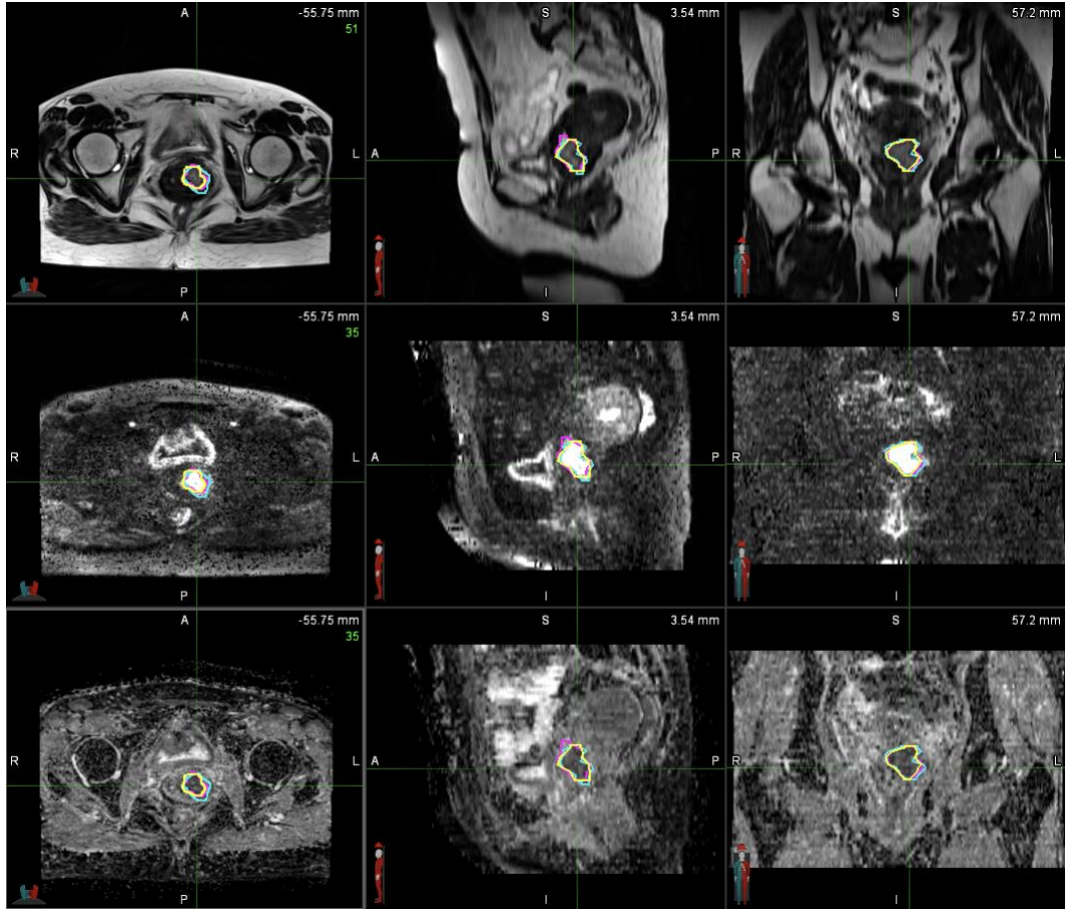
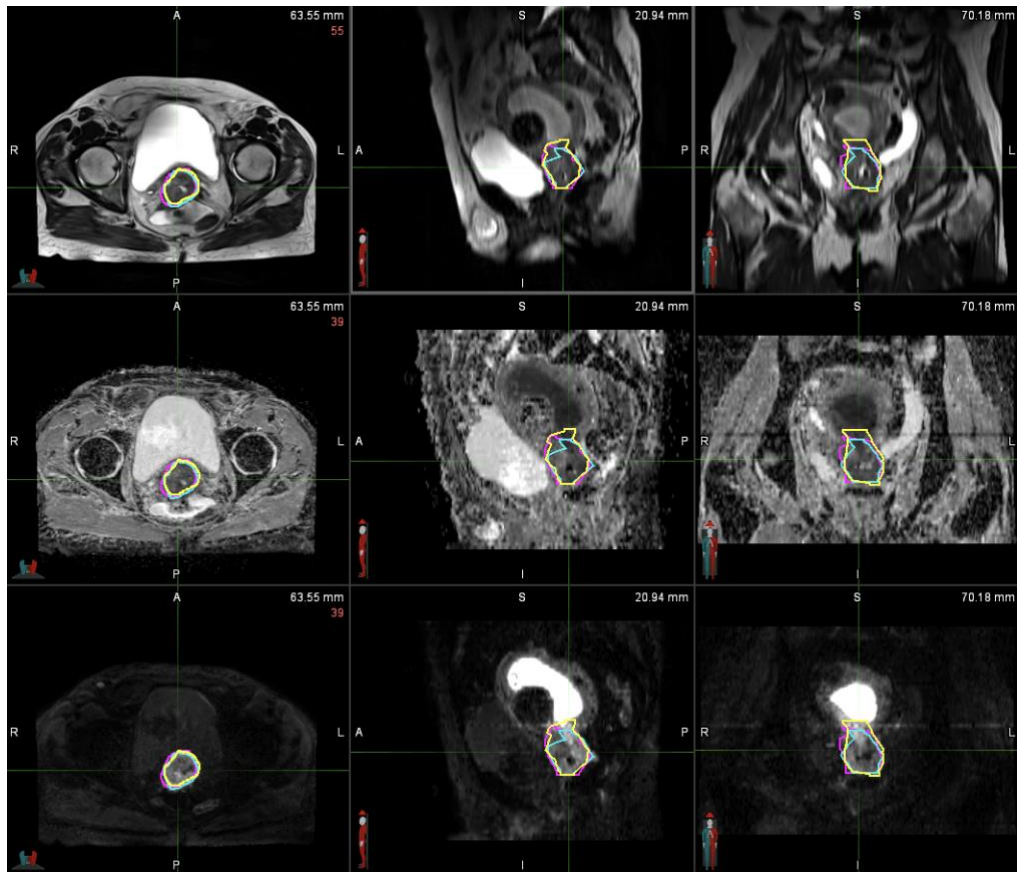


**Figure A3: Example slice from Patient 4's a) pre-EBRT scan and b) pre-brachytherapy scan with the overlaid GTVs. The image rows from top to bottom for both scans are T2 MRI, DWI, and ADC. The GTVs contoured with the axial T2 MRI, with the axial T2 MRI/DWI fusion, and with the axial T2 MRI/ADC fusion are magenta, cyan, and yellow, respectively.**

a)



b)

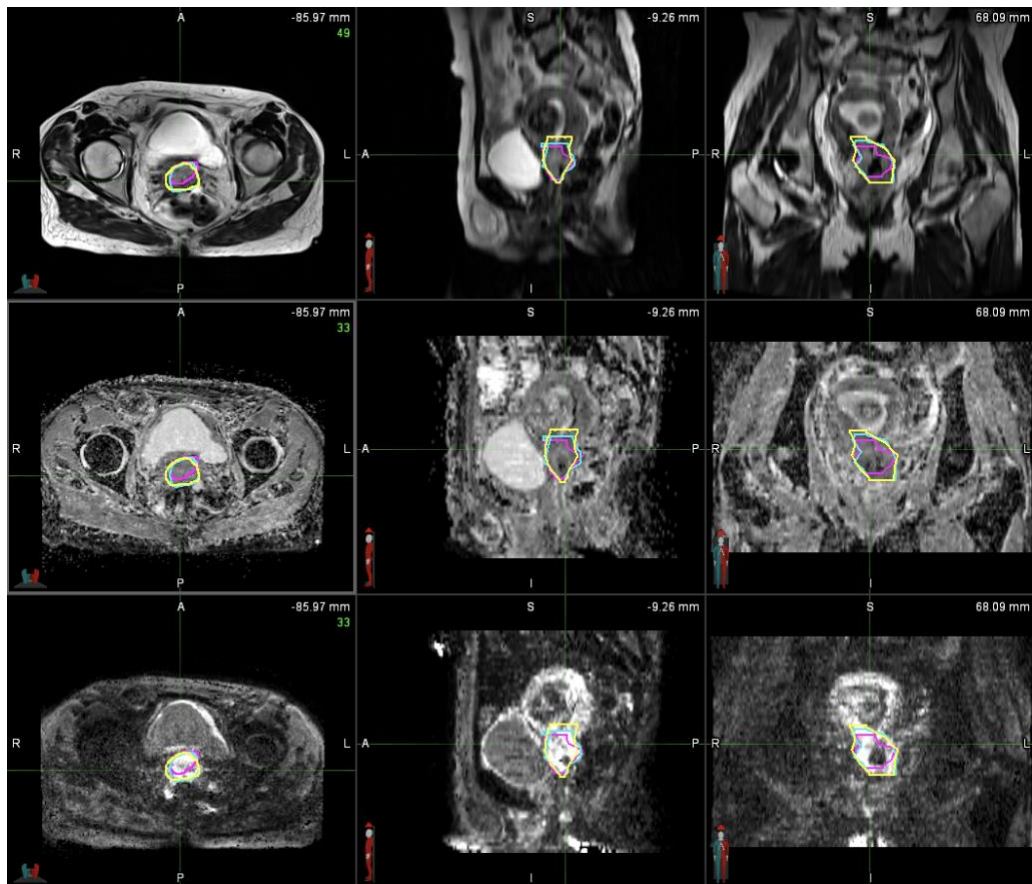
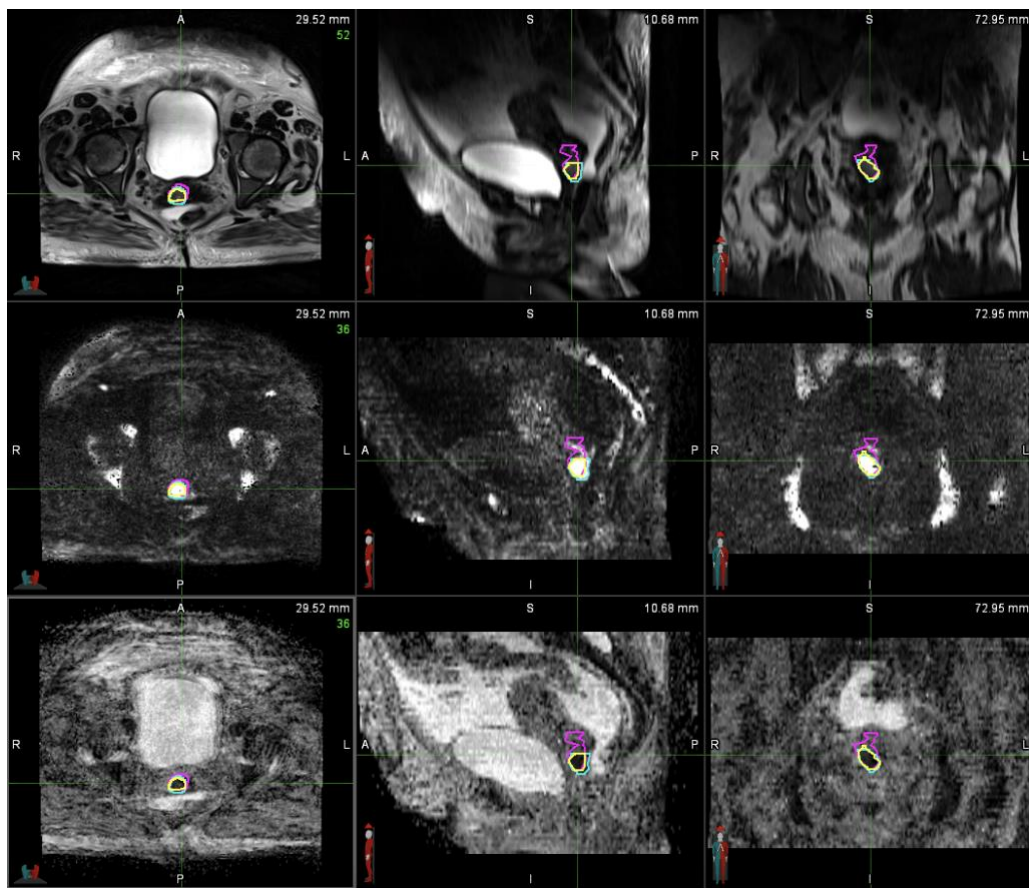


**Figure A4: Example slice from Patient 5's a) pre-EBRT scan and b) pre-brachytherapy scan with the overlaid GTVs. The image rows from top to bottom for both scans are T2 MRI, ADC, and DWI. The GTVs contoured with the axial T2 MRI, with the axial T2 MRI/DWI fusion, and with the axial T2 MRI/ADC fusion are magenta, cyan, and yellow, respectively.**

a)



b)

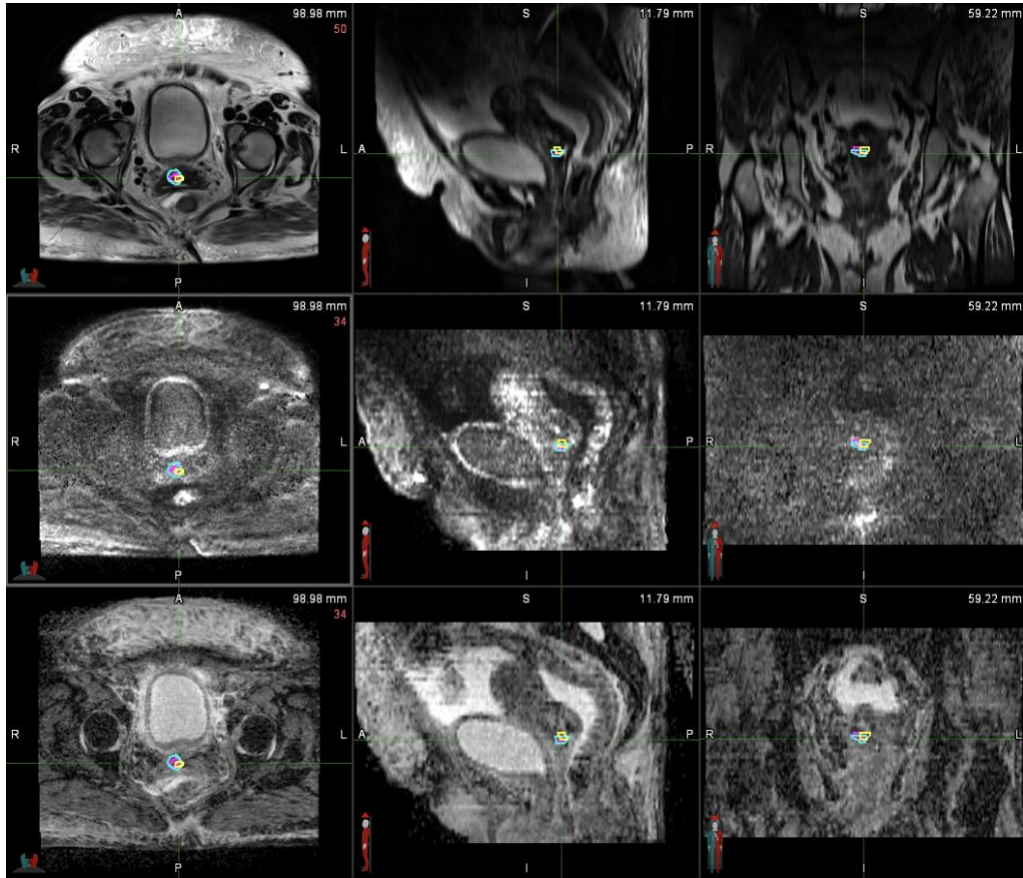


**Figure A5: Example slice from Patient 6's a) pre-EBRT scan and b) pre-brachytherapy scan with the overlaid GTVs. The image rows from top to bottom for both scans are T2 MRI, DWI, and ADC. The GTVs contoured with the axial T2 MRI, with the axial T2 MRI/DWI fusion, and with the axial T2 MRI/ADC fusion are magenta, cyan, and yellow, respectively.**

## References

- American Society for Radiation Oncology. (2020). *Rtanswers*. Radiation Therapy for Gynecologic Cancers. <https://www.rtanswers.org/RTAnswers/media/RTAnswers/patient%20materials/PDFs/GYNCancers.pdf>
- Amine. (2021, September 28). *The difference between dice and Dice Loss*. PYCAD. <https://pycad.co/the-difference-between-dice-and-dice-loss/>
- Arlinghaus, L. R., & Yankeelov, T. E. (2012). Diffusion-Weighted MRI. In *Quantitative MRI in Cancer*. Essay, Taylor & Francis Group.
- Bakiu, E., Telhaj, E., Kozma, E., Ruci, F., & Malkaj, P. (2013). Comparison of 3D CRT and IMRT Treatment plans. *Acta Informatica Medica*, 21(3), 211. <https://doi.org/10.5455/aim.2013.21.211-212>
- Bennett, K. M., Schmainda, K. M., Bennett, R. T., Rowe, D. B., Lu, H., & Hyde, J. S. (2003). Characterization of continuously distributed cortical water diffusion rates with a stretched-exponential model. *Magnetic resonance in medicine*, 50(4), 727–734. <https://doi.org/10.1002/mrm.10581>
- Bruegel, M., Holzapfel, K., Gaa, J., Woertler, K., Waldt, S., Kiefer, B., Stemmer, A., Ganter, C., & Rummeny, E. J. (2008). Characterization of focal liver lesions by ADC measurements using a respiratory triggered diffusion-weighted single-shot echo-planar MR imaging technique. *European radiology*, 18(3), 477–485. <https://doi.org/10.1007/s00330-007-0785-9>
- BXTA. (2023, March 29). *The difference between LDR and HDR Brachytherapy*. <https://bxta.com/uk/ldr-and-hdr-brachytherapy/>
- Centers for Disease Control and Prevention. (2023, June 13). *How are gynecologic cancers treated?*. Centers for Disease Control and Prevention. [https://www.cdc.gov/cancer/gynecologic/basic\\_info/treatment.htm#:~:text=Treatments%20may%20include%20surgery%2C%20chemotherapy,shrink%20or%20kill%20the%20cancer.](https://www.cdc.gov/cancer/gynecologic/basic_info/treatment.htm#:~:text=Treatments%20may%20include%20surgery%2C%20chemotherapy,shrink%20or%20kill%20the%20cancer.)
- Centers for Disease Control and Prevention. Gynecologic Cancer Incidence, United States—2012–2016. USCS Data Brief, no 11. Atlanta, GA: Centers for Disease Control and Prevention, US Department of Health and Human Services; 2019.

- Chenevert, T.L., Galbán, C.J., Ivancevic, M.K., Rohrer, S.E., Londy, F.J., Kwee, T.C., Meyer, C.R., Johnson, T.D., Rehemtulla, A. and Ross, B.D. (2011), Diffusion coefficient measurement using a temperature-controlled fluid for quality control in multicenter studies. *J. Magn. Reson. Imaging*, 34: 983-987. <https://doi.org/10.1002/jmri.22363>
- Dalah, E., Erickson, B., Oshima, K., Schott, D., Hall, W. A., Paulson, E., Tai, A., Knechtges, P., & Li, X. A. (2018). Correlation of ADC With Pathological Treatment Response for Radiation Therapy of Pancreatic Cancer. *Translational oncology*, 11(2), 391–398. <https://doi.org/10.1016/j.tranon.2018.01.018>
- Dappa, E., Elger, T., Hasenburg, A., Düber, C., Battista, M. J., & Hötter, A. M. (2017). The value of advanced MRI techniques in the assessment of Cervical Cancer: A Review. *Insights into Imaging*, 8(5), 471–481. <https://doi.org/10.1007/s13244-017-0567-0>
- Feng, C. H., Hasan, Y., Kopec, M., & Al-Hallaq, H. A. (2016). Simultaneously integrated boost (SIB) spares oar and reduces treatment time in locally advanced cervical cancer. *Journal of Applied Clinical Medical Physics*, 17(5), 76–89. <https://doi.org/10.1120/jacmp.v17i5.6123>
- Fujii S, Matsusue E, Kigawa J, et al. Diagnostic accuracy of the apparent diffusion coefficient in differentiating benign from malignant uterine endometrial cavity lesions: initial results. *Eur Radiol* 2008;18:384–389
- Gladwish, A., Milosevic, M., Fyles, A., Xie, J., Halankar, J., Metser, U., Jiang, H., Becker, N., Levin, W., Manchul, L., Foltz, W., & Han, K. (2016). Association of apparent diffusion coefficient with disease recurrence in patients with locally advanced cervical cancer treated with radical chemotherapy and radiation therapy. *Radiology*, 279(1), 158–166. <https://doi.org/10.1148/radiol.2015150400>
- Grigsby PW, Portelance L, Williamson JF. High dose ratio (HDR) cervical ring applicator to control bleeding from cervical carcinoma. *International journal of gynecological cancer: official journal of the International Gynecological Cancer Society*. 2002;12:18–21.
- Guo, Y., Cai, Y. Q., Cai, Z. L., Gao, Y. G., An, N. Y., Ma, L., Mahankali, S., & Gao, J. H. (2002). Differentiation of clinically benign and malignant breast lesions using diffusion-weighted imaging. *Journal of magnetic resonance imaging: JMRI*, 16(2), 172–178. <https://doi.org/10.1002/jmri.10140>

- Gynecological cancers - Foundation for Women's Cancer*. Foundation For Women's Cancer - Eradicate or lessen the impact of gynecologic cancer. (2024, March 12). <https://foundationforwomenscancer.org/gynecological-cancers/>
- Haack, S., Pedersen, E. M., Jespersen, S. N., Kallehauge, J. F., Lindegaard, J. C., & Tanderup, K. (2010). Apparent diffusion coefficients in GEC ESTRO target volumes for image guided adaptive brachytherapy of locally advanced cervical cancer. *Acta Oncologica*, 49(7), 978–983. <https://doi.org/10.3109/0284186x.2010.500619>
- Haider, M. A., van der Kwast, T. H., Tanguay, J., Evans, A. J., Hashmi, A.-T., Lockwood, G., & Trachtenberg, J. (2007). Combined T2-weighted and diffusion-weighted MRI for localization of prostate cancer. *American Journal of Roentgenology*, 189(2), 323–328. <https://doi.org/10.2214/ajr.07.2211>
- Haie-Meder, C., Pötter, R., Van Limbergen, E., Briot, E., De Brabandere, M., Dimopoulos, J., Dumas, I., Hellebust, T. P., Kirisits, C., Lang, S., Muschitz, S., Nevinson, J., Nulens, A., Petrow, P., & Wachter-Gerstner, N. (2005). Recommendations from Gynaecological (GYN) GEC-ESTRO Working Group☆ (I): Concepts and terms in 3D image based 3D treatment planning in cervix cancer brachytherapy with emphasis on MRI assessment of GTV and CTV. *Radiotherapy and Oncology*, 74(3), 235–245. <https://doi.org/10.1016/j.radonc.2004.12.015>
- Hall, M. G. (2016, August 9). *Continuity, the Bloch-Torrey equation, and diffusion MRI*. arXiv.org. <https://arxiv.org/abs/1608.02859>
- Han K, Milosevic M, Fyles A, Pintilie M, Viswanathan AN. Trends in the utilization of brachytherapy in cervical cancer in the United States. *International journal of radiation oncology, biology, physics*. 2013;87:111–9.
- Harkenrider, M. M., Albuquerque, K., Brown, D., Kamrava, M., King, M., Mourtada, F., Orio, P., Patel, R., Price, M., Rassiah, P., Solanki, A. A., Small, W., & Schechter, N. R. (2021). ACR-abs-astro practice parameter for the performance of radionuclide-based high-dose-rate brachytherapy. *Brachytherapy*, 20(6), 1071–1082. <https://doi.org/10.1016/j.brachy.2021.08.009>
- Ho, J. C., Allen, P. K., Bhosale, P. R., Rauch, G. M., Fuller, C. D., Mohamed, A. S., Frumovitz, M., Jhingran, A., & Klopp, A. H. (2017). Diffusion-Weighted Magnetic Resonance Imaging as a Predictor of Outcome in Cervical Cancer After Chemoradiation. *International journal of radiation oncology, biology, physics*, 97(3), 546–553. <https://doi.org/10.1016/j.ijrobp.2016.11.015>

- Huang, L., Snyder, A. R., & Morgan, W. F. (2003). Radiation-induced genomic instability and its implications for radiation carcinogenesis. *Oncogene*, 22(37), 5848–5854. <https://doi.org/10.1038/sj.onc.1206697>
- Kuang F, Yan Z, Wang J, Rao Z (2014) The value of diffusion-weighted MRI to evaluate the response to radiochemotherapy for cervical cancer. *Magn Reson Imaging* 32:342–349
- Kumar, R., Narayanan, G. S., Vishwanthan, B., Narayanan, S., & Mandal, S. (2020). Aprospective comparative dosimetric study between diffusion weighted MRI (DWI) & T2-weighted MRI (T2W) for target delineation and planning in cervical cancer brachytherapy. *Reports of Practical Oncology & Radiotherapy*, 25(6), 1011–1016. <https://doi.org/10.1016/j.rpor.2020.08.008>
- Liu Y, Bai R, Sun H, Liu H, Wang D. Diffusion-weighted magnetic resonance imaging of uterine cervical cancer. *J Comput Assist Tomogr*. 2009 Nov-Dec;33(6):858-62. doi: 10.1097/RCT.0b013e31819e93af. PMID: 19940650.
- Mackenzie, R. J. (2018, July 20). *One-way vs two-way ANOVA: Differences, assumptions and hypotheses*. Informatics from Technology Networks. <https://www.technologynetworks.com/informatics/articles/one-way-vs-two-way-anova-definition-differences-assumptions-and-hypotheses-306553>
- Mai, J., Erickson, B., Rownd, J., & Gillin, M. (2001). Comparison of four different dose specification methods for high-dose-rate intracavitary radiation for treatment of cervical cancer. *International journal of radiation oncology, biology, physics*, 51(4), 1131–1141. [https://doi.org/10.1016/s0360-3016\(01\)01771-0](https://doi.org/10.1016/s0360-3016(01)01771-0)
- Mayo Foundation for Medical Education and Research. (2022, January 6). *CT Scan*. Mayo Clinic. <https://www.mayoclinic.org/tests-procedures/ct-scan/about/pac-20393675>
- Mayo Foundation for Medical Education and Research. (2023, April 18). *Positron Emission Tomography Scan*. Mayo Clinic. <https://www.mayoclinic.org/tests-procedures/pet-scan/about/pac-20385078>
- McClenaghan, E. (2023, February 20). *The Wilcoxon signed-rank test*. Informatics from Technology Networks. <https://www.technologynetworks.com/informatics/articles/the-wilcoxon-signed-rank-test-370384>

- Moribata, Y., Kido, A., Fujimoto, K., Himoto, Y., Kurata, Y., Shitano, F., Kiguchi, K., Konishi, I., & Togashi, K. (2017). Feasibility of Computed Diffusion Weighted Imaging and Optimization of b-value in Cervical Cancer. *Magnetic resonance in medical sciences : MRMS : an official journal of Japan Society of Magnetic Resonance in Medicine*, *16*(1), 66–72. <https://doi.org/10.2463/mrms.mp.2015-0161>
- Motoshima, S., Irie, H., Nakazono, T., Kamura, T., & Kudo, S. (2011). Diffusion-weighted MR imaging in gynecologic cancers. *Journal of gynecologic oncology*, *22*(4), 275–287. <https://doi.org/10.3802/jgo.2011.22.4.275>
- Mukuda, N., Fujii, S., Inoue, C., Fukunaga, T., Tanabe, Y., Itamochi, H., & Ogawa, T. (2016). Apparent diffusion coefficient (ADC) measurement in ovarian tumor: Effect of region-of-interest methods on ADC values and diagnostic ability. *Journal of magnetic resonance imaging : JMRI*, *43*(3), 720–725. <https://doi.org/10.1002/jmri.25011>
- Murakami, N., Kobayashi, K., Shima, S., Tsuchida, K., Kashihara, T., Tselis, N., Umezawa, R., Takahashi, K., Inaba, K., Ito, Y., Igaki, H., Nakayama, Y., Masui, K., Yoshida, K., Kato, T., & Itami, J. (2019). A hybrid technique of intracavitary and interstitial brachytherapy for locally advanced cervical cancer: Initial outcomes of a single-institute experience. *BMC Cancer*, *19*(1). <https://doi.org/10.1186/s12885-019-5430-x>
- Nag, S. (2004). High dose rate brachytherapy: Its clinical applications and treatment guidelines. *Technology in Cancer Research & Treatment*, *3*(3), 269–287. <https://doi.org/10.1177/153303460400300305>
- Naganawa, S., Sato, C., Kumada, H. *et al.* Apparent diffusion coefficient in cervical cancer of the uterus: comparison with the normal uterine cervix. *Eur Radiol* **15**, 71–78 (2005). <https://doi.org/10.1007/s00330-004-2529-4>
- Onodera, K., Hatakenaka, M., Yama, N., Onodera, M., Saito, T., Kwee, T. C., & Takahara, T. (2019). Repeatability analysis of ADC histogram metrics of the uterus. *Acta radiologica (Stockholm, Sweden : 1987)*, *60*(4), 526–534. <https://doi.org/10.1177/0284185118786062>
- Ozcan, A., Wong, K. H., Larson-Prior, L., Cho, Z. H., & Mun, S. K. (2012). Background and Mathematical Analysis of Diffusion MRI Methods. *International journal of imaging systems and technology*, *22*(1), 44–52. <https://doi.org/10.1002/ima.22001>

- Pickens, David (2012) Image Formation. In Quantitative MRI in Cancer. Essay, Taylor & Francis Group.
- Pötter R, Tanderup K, Schmid MP, *et al.* MRI-guided adaptive brachytherapy in locally advanced cervical cancer (EMBRACE-I): a multicentre prospective cohort study. *Lancet Oncol* 2021;22:538–47.
- Quan, E. M., Li, X., Li, Y., Wang, X., Kudchadker, R. J., Johnson, J. L., Kuban, D. A., Lee, A. K., & Zhang, X. (2012). A comprehensive comparison of IMRT and VMAT plan quality for prostate cancer treatment. *International Journal of Radiation Oncology\*Biophysics*, 83(4), 1169–1178.  
<https://doi.org/10.1016/j.ijrobp.2011.09.015>
- Rosa, C., Pizzi, A., Augurio, A., Caravatta, L., Di Tommaso, M., Mincuzzi, E., Cinalli, S., Basilico, R., Porreca, A., Di Nicola, M., & Genovesi, D. (2020). Volume delineation in cervical cancer with T2 and diffusion-weighted MRI: Agreement on volumes between observers. *In Vivo*, 34(4), 1981–1986.  
<https://doi.org/10.21873/invivo.11995>
- Sarah Cannon Cancer Institute. (n.d.). *Types of radiation therapy*. Sarah Cannon.  
<https://sarahcannon.com/service/types-of-radiation-therapy>
- Siegel, R. L., Miller, K. D., Fuchs, H. E., & Jemal, A. (2021). Cancer Statistics, 2021. *CA Cancer J Clin*, 71(1), 7-33
- Smith, Seth (2012). Physics of MRI. In Quantitative MRI in Cancer. Essay, Taylor & Francis Group.
- Soliman, A. S., Owrangi, A., Ravi, A., & Song, W. Y. (2016). Metal artefacts in MRI-guided brachytherapy of cervical cancer. *Journal of Contemporary Brachytherapy*, 4, 363–369. <https://doi.org/10.5114/jcb.2016.61817>
- Song J, Lu Y, Wang X, *et al.* A comparative study of four diffusion-weighted imaging models in the diagnosis of cervical cancer. *Acta Radiologica*. 2022;63(4):536-544.  
 doi:10.1177/02841851211002017
- Søren Haack, Jesper F. Kallehauge, Sune N. Jespersen, Jacob C. Lindegaard, Kari Tanderup & Erik M. Pedersen (2014) Correction of diffusion-weighted magnetic resonance imaging for brachytherapy of locally advanced cervical cancer, *Acta Oncologica*, 53:8, 1073-1078, DOI: [10.3109/0284186X.2014.938831](https://doi.org/10.3109/0284186X.2014.938831)

- Stejskal, E. O., & Tanner, J. E. (1965). Spin diffusion measurements: Spin echoes in the presence of a time-dependent field gradient. *The Journal of Chemical Physics*, *42*(1), 288–292. <https://doi.org/10.1063/1.1695690>
- Stewart, A. J., & Viswanathan, A. N. (2006). Current controversies in high-dose-rate versus low-dose-rate brachytherapy for cervical cancer. *Cancer*, *107*(5), 908–915. <https://doi.org/10.1002/cncr.22054>
- Tamai K, Koyama T, Saga T, et al. The utility of diffusion-weighted MR imaging for differentiating uterine sarcomas from benign leiomyomas. *Eur Radiol* 2008;18:723–730.
- Tanderup, K., Viswanathan, A. N., Kirisits, C., & Frank, S. J. (2014). Magnetic Resonance Image Guided Brachytherapy. *Seminars in Radiation Oncology*, *24*(3), 181–191. <https://doi.org/10.1016/j.semradonc.2014.02.007>
- Uniqtech. (2020, August 20). *Understand Jaccard Index, Jaccard similarity in minutes*. Medium. <https://medium.com/data-science-bootcamp/understand-jaccard-index-jaccard-similarity-in-minutes-25a703fbf9d7>
- Vergalaso, I., Light, K., Chino, J., & Craciunescu, O. (2017). Simultaneous integrated boost (SIB) for treatment of gynecologic carcinoma: Intensity-modulated radiation therapy (IMRT) vs Volumetric-modulated arc therapy (VMAT) radiotherapy. *Medical Dosimetry*, *42*(3), 230–237. <https://doi.org/10.1016/j.meddos.2017.05.002>
- Viani, G. A., Manta, G. B., Stefano, E. J., & de Fendi, L. I. (2009). Brachytherapy for cervix cancer: low-dose rate or high-dose rate brachytherapy - a meta-analysis of clinical trials. *Journal of experimental & clinical cancer research : CR*, *28*(1), 47. <https://doi.org/10.1186/1756-9966-28-47>
- Viswanathan, A. N., Beriwal, S., De Los Santos, J. F., Demanes, D. J., Gaffney, D., Hansen, J., Jones, E., Kirisits, C., Thomadsen, B., Erickson, B., & American Brachytherapy Society (2012). American Brachytherapy Society consensus guidelines for locally advanced carcinoma of the cervix. Part II: high-dose-rate brachytherapy. *Brachytherapy*, *11*(1), 47–52. <https://doi.org/10.1016/j.brachy.2011.07.002>
- Williamson, C. W., Liu, H. C., Mayadev, J., & Mell, L. K. (2021). Advances in external beam radiation therapy and brachytherapy for cervical cancer. *Clinical Oncology*, *33*(9), 567–578. <https://doi.org/10.1016/j.clon.2021.06.012>

- Woodhouse, K. D., Devlin, P. M., Kollmeier, M., Lin, L. L., Orio, P., Ouhib, Z., Song, D., Viswanathan, A. N., Watanabe, Y., Yu, Y., Small, W., & Schechter, N. R. (2022). ACR-ABS-astro practice parameter for the performance of low-dose-rate brachytherapy. *American Journal of Clinical Oncology*, *45*(6), 243–248. <https://doi.org/10.1097/coc.0000000000000912>
- Yoshida, K., Yamazaki, H., Kotsuma, T., Takenaka, T., Ueda, M. M., Miyake, S., Tsujimoto, Y., Masui, K., Yoshioka, Y., Sumida, I., Uesugi, Y., Shimbo, T., Yoshikawa, N., Yoshioka, H., Tanaka, E., & Narumi, Y. (2016). Simulation analysis of optimized brachytherapy for uterine cervical cancer: Can we select the best brachytherapy modality depending on tumor size? *Brachytherapy*, *15*(1), 57–64. <https://doi.org/10.1016/j.brachy.2015.10.002>
- Zhou, Y., Gu, H.-L., Zhang, X.-L., Tian, Z.-F., Xu, X.-Q., & Tang, W.-W. (2021). Multiparametric magnetic resonance imaging-derived radiomics for the prediction of disease-free survival in early-stage squamous cervical cancer. *European Radiology*, *32*(4), 2540–2551. <https://doi.org/10.1007/s00330-021-08326-6>